



Calibration of an airborne HO_x instrument using the All Pressure Altitude-based Calibrator for HO_x Experimentation (APACHE)

Daniel Marno¹, Cheryl Ernest^{1,a}, Korbinian Hens^{1,b}, Umar Javed^{1,2}, Thomas Klimach¹, Monica Martinez¹, Markus Rudolf¹, Jos Lelieveld¹, and Hartwig Harder¹

¹Atmospheric Chemistry Department, Max Planck Institute for Chemistry, 55128 Mainz, Germany

²Forschungszentrum Jülich GmbH, IEK-8, 52425 Jülich, Germany

^anow at: Department of Neurology, University Medical Center of the Johannes Gutenberg University Mainz, 55131 Mainz, Germany

^bnow at: Hübner GmbH & Co KG – Division Hübner Photonics, 34123 Kassel, Germany

Correspondence: Daniel Marno (daniel.marno@mpic.de) and Hartwig Harder (hartwig.harder@mpic.de)

Received: 18 November 2019 – Discussion started: 26 November 2019

Revised: 26 February 2020 – Accepted: 3 April 2020 – Published: 27 May 2020

Abstract. Laser-induced fluorescence (LIF) is a widely used technique for both laboratory-based and ambient atmospheric chemistry measurements. However, LIF instruments require calibrations in order to translate instrument response into concentrations of chemical species. Calibration of LIF instruments measuring OH and HO₂ (HO_x) typically involves the photolysis of water vapor by 184.9 nm light, thereby producing quantitative amounts of OH and HO₂. For ground-based HO_x instruments, this method of calibration is done at one pressure (typically ambient pressure) at the instrument inlet. However, airborne HO_x instruments can experience varying cell pressures, internal residence times, temperatures, and humidity during flight. Therefore, replication of such variances when calibrating in the lab is essential to acquire the appropriate sensitivities. This requirement resulted in the development of the APACHE (All Pressure Altitude-based Calibrator for HO_x Experimentation) chamber to characterize the sensitivity of the airborne LIF-FAGE (fluorescence assay by gas expansion) HO_x instrument, HORUS, which took part in an intensive airborne campaign, OMO-Asia 2015. It utilizes photolysis of water vapor but has the additional ability to alter the pressure at the nozzle of the HORUS instrument. With APACHE, the HORUS instrument sensitivity towards OH (26.1–7.8 cts s^{−1} pptv^{−1} mW^{−1}, ±22.6 % 1σ; cts stands for counts by the detector) and HO₂ (21.2–8.1 cts s^{−1} pptv^{−1} mW^{−1}, ±22.1 % 1σ) was characterized to the external pressure range at the instrument nozzle of 227–900 mbar. Measure-

ments supported by a computational fluid dynamics model, COMSOL Multiphysics, revealed that, for all pressures explored in this study, APACHE is capable of initializing a homogenous flow and maintaining near-uniform flow speeds across the internal cross section of the chamber. This reduces the uncertainty regarding average exposure times across the mercury (Hg) UV ring lamp. Two different actinometrical approaches characterized the APACHE UV ring lamp flux as $6.37 \times 10^{14} (\pm 1.3 \times 10^{14})$ photons cm^{−2} s^{−1}. One approach used the HORUS instrument as a transfer standard in conjunction with a calibrated on-ground calibration system traceable to NIST standards, which characterized the UV ring lamp flux to be $6.9 (\pm 1.1) \times 10^{14}$ photons cm^{−2} s^{−1}. The second approach involved measuring ozone production by the UV ring lamp using an ANSYCO O3 41 M ozone monitor, which characterized the UV ring lamp flux to be $6.11 (\pm 0.8) \times 10^{14}$ photons cm^{−2} s^{−1}. Data presented in this study are the first direct calibrations of an airborne HO_x instrument, performed in a controlled environment in the lab using APACHE.

1 Introduction

It is well known that the hydroxyl (OH) radical is a potent oxidizing agent in daytime photochemical degradation of pollutants sourced from anthropogenic and biogenic processes, thus accelerating their removal from our atmosphere. The hy-

droperoxyl radical (HO_2) also plays a central role in atmospheric oxidation as it not only acts as a reservoir for OH but is involved in formation of other oxidants such as peroxides and impacts the cycling of pollutants such as NO_x ($=\text{NO} + \text{NO}_2$) (Lelieveld et al., 2002). Therefore, measurements of OH and HO_2 (HO_x) within the troposphere are essential in understanding the potential global-scale impacts of pollutants in both the present day and in climate predictions. One common HO_x measurement method is laser-induced fluorescence (LIF) (Stevens et al., 1994; Brune et al., 1995; Hard et al., 1995; Martinez et al., 2003; Faloona et al., 2004; Stone et al., 2010; Hens et al., 2014; Novelli et al., 2014). Other methods have been successfully implemented to measure HO_x . Chemical ionization mass spectrometry (CIMS) (Cantrell et al., 2003; Mauldin et al., 2004; Sjostedt et al., 2007; Dusanter et al., 2008; Kukui et al., 2008; Albrecht et al., 2019) and differential optical absorption spectroscopy (DOAS) (Brauers et al., 1996, 2001; Schlosser et al., 2007) have also been used in the measurement of HO_x in the field and in intercomparison projects with LIF instrumentation. However, low atmospheric concentrations of HO_x (Schlosser et al., 2009) and potential interferences (Faloona et al., 2004; Fuchs et al., 2011, 2016; Mao et al., 2012; Hens et al., 2014; Novelli et al., 2014) can make HO_x measurements especially challenging. Airborne LIF-FAGE (LIF–fluorescence assay by gas expansion) instruments experience large variability in pressure, humidity, instrument internal air density, and internal quenching during flights, which cause a wide array of instrumental sensitivities (Faloona et al., 2004; Martinez et al., 2010; Regelin et al., 2013; Winiberg et al., 2015). Therefore, it is critical to utilize a calibration system that can suitably reproduce in-flight conditions to determine the instrument response to known levels of OH and HO_2 to acquire robust HO_x measurements.

The first stage of the Hydroxyl Radical measurement Unit based on fluorescence Spectroscopy (HORUS) inlet is an inlet preinjector (IPI), used to determine the concentration of background OH interferences by removing atmospheric OH from the signal via addition of an OH scavenger such as propane. IPI draws $50\text{--}230\text{ sL min}^{-1}$ depending on altitude and is susceptible to temperature- and pressure-driven changes in internal reaction rates and residence times under flight conditions. This has implications for the removal of atmospheric OH in the inlet and for the characterization of background interference signals in HORUS. Therefore, a device capable of providing stable high flows while reproducing a wide range of pressures and temperatures is needed in order to calibrate the airborne HORUS instrument. This led to the production, characterization, and utilization of the calibration device APACHE (All Pressure Altitude-based Calibrator for HO_x Experimentation) which is described in depth in this work.

2 Experimental design and setup

2.1 APACHE design overview

Figure 1 shows the overview of the APACHE system. In front of the APACHE inlet, a series of mixing blocks are installed where multiple dry synthetic air additions are injected into a controlled humidified air supply ensuring thorough mixing of water vapor before being measured by a LI-COR 6262 $\text{CO}_2/\text{H}_2\text{O}$ (Fig. 1a). This air is then fed into a large mass flow controller (MFC). The construction of the APACHE chamber itself is shown in Fig. 1b. The first section contains the diffuser inlet with a sintered filter (bronze alloy, Amtag, filter class 10). This 2 mm thick sintered filter, with a pore size of $35\text{ }\mu\text{m}$, initializes a homogeneous flow and further improves the mixing of water vapor in front of the UV ring lamp (described further in Sect. 4). The water photolysis section contains a low-pressure, 0.8 A, mercury ring lamp (uv-technik; see Fig. S1 in the Supplement) which produces a constant radial photon flux at 184.9 nm, situated 133 mm after the sintered filter and separated from the main APACHE chamber by an airtight quartz window. Between the lamp and the quartz window there is an anodized aluminum band with thirty 8 mm apertures blocking all light apart from that going through the apertures, which reduces the amount of UV flux entering APACHE and limits the size of the illuminated area. The IPI system is clamped down 169.5 mm behind the photolysis section in such a way that the instrument sample flow is perpendicular to the airflow passing over the IPI nozzle. The nozzle protrudes 51.5 mm into the APACHE cavity much like it is when installed in the aircraft shroud system (see Fig. 2), and it is made airtight with the use of O-rings. Opposite the IPI nozzle, there is an airtight block attachment containing a series of monitoring systems. A pitot tube attached to an Airflow PTSX-K 0–10Pa differential pressure sensor (accuracy rating of 1 % at full scale, 1σ) is used to monitor the internal flow speeds within APACHE. A $3\text{ k}\Omega$ NTC-EC95302V thermistor is used to monitor the air temperature, and an Edwards ASG2-1000 pressure sensor (with an accuracy rating of $\pm 4\text{ mbar}$, 2σ) monitors the static air pressure. Additionally, there are two $1/4\text{ in.}$ (6.35 mm) airtight apertures in the monitoring block that can be opened to enable other instrumentation to be installed.

2.2 Pressure control

For this study, the operational pressure range of APACHE used was 227–900 mbar, with a precision of $\pm 0.1\text{ }\%$ (1σ) and accuracy of $\pm 2\text{ }\%$ (1σ) and with mass flows ranging from 200 to 990 sL min^{-1} (sL stands for standard liter). This was achieved using an Edwards GSX160 scroll pump controlling the volume flow in combination with a MFC (Bronkhorst F-601A1-PAD-03-V) controlling the mass flow of air entering APACHE. This system reached air speeds of $0.9\text{ to }1.5\text{ m s}^{-1}$ through APACHE at pressures ranging from 250 to 900 mbar

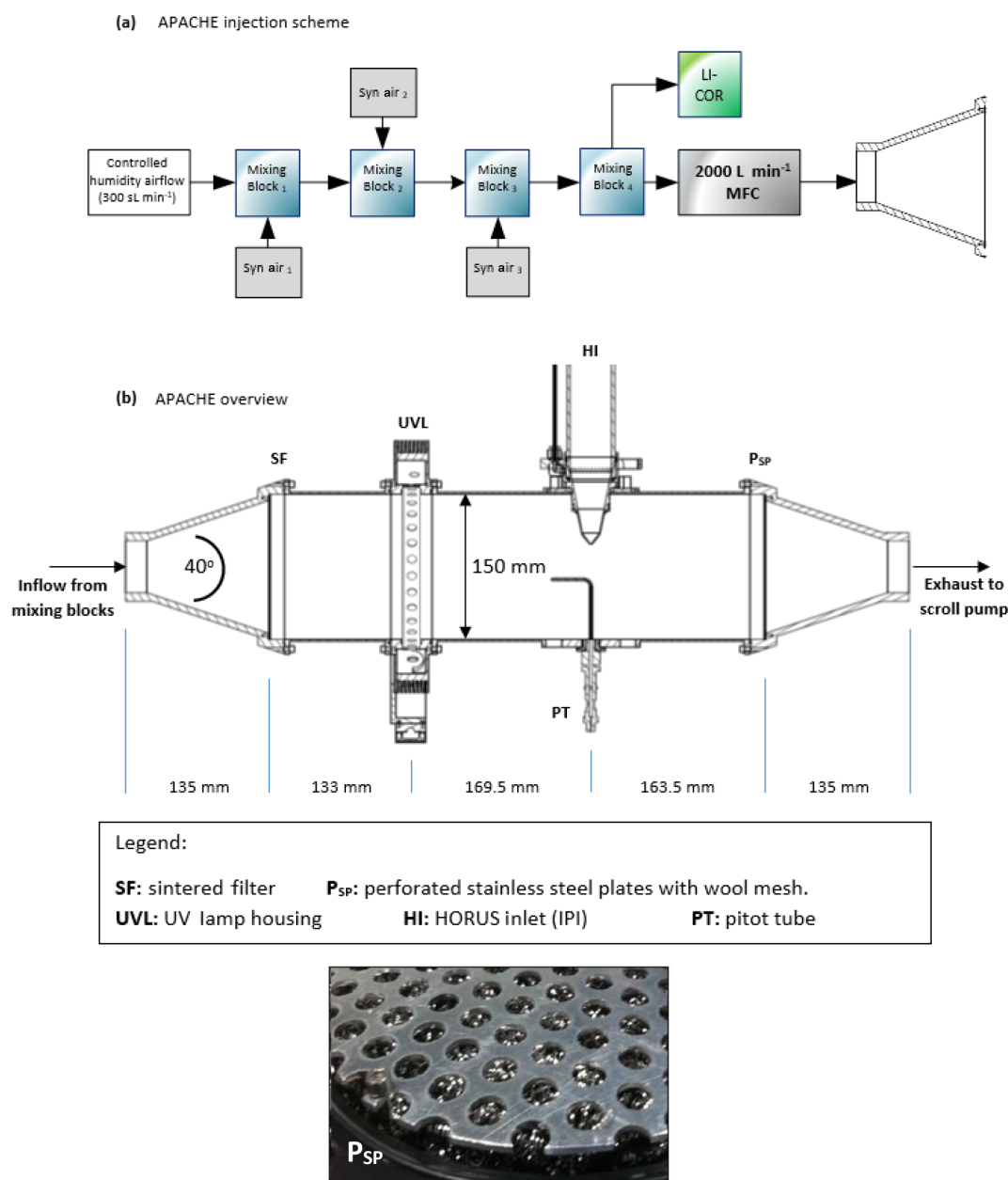


Figure 1. Overview of the APACHE system and the premixing setup used in the lab to calibrate the HORUS airborne instrument. A picture at the bottom shows the perforated stainless-steel plates with wool mesh.

and at temperatures ranging from 282 to 302 K. Temperature changes inside APACHE are not controlled. However, as air temperature is measured throughout the calibration device and HORUS, any term that is affected by temperature is characterized using the corresponding measured temperature values. Although not critical for this study, the operational pressure range of APACHE can be extended by changing the draw speed of the Edwards scroll pump. However, that may cause the flow speeds and potentially the flow speed profiles across the UV ring lamp to vary in between different pressure calibrations.

2.3 The airborne HORUS instrument

The LIF-FAGE instrument developed by our group (HORUS) is based on the original design of GTHOS (Ground-based Tropospheric Hydrogen Oxides Sensor) described by Faloona et al. (2004) and is described in further detail by Martinez et al. (2010). The airborne instrument is a revised and altered design to perform under conditions experienced during flight and conform to aeronautical regulations. It was primarily developed for installation on the High Altitude and Long Range Research Aircraft (HALO) and took place in the

OMO-Asia 2015 airborne campaign. The system comprises of an external inlet shroud, detection axes, a laser system, and a vacuum system (Fig. 2). Additionally, this is the first airborne LIF-FAGE instrument measuring HO_x with a dedicated inlet preinjector (IPI) system installed for the purpose of removing atmospheric OH, enabling real-time measurements and quantification of potential chemical background OH interferences, OH-CHEM (Mao et al., 2012). The airborne IPI system is redesigned to fit within the shroud inlet system, and its walls are heated to 30°C , while maintaining similar operational features to the on-ground IPI installation (Novelli et al., 2014). To prevent excessive collisions of OH and HO_2 with the IPI nozzle and internal walls, thus limiting losses of HO_x during flight, the momentum inertia of the air passing through the external shroud system had to be overcome to promote flow direction into the instrument. This was achieved by installing a choke point behind the IPI nozzle in the inlet shroud, resulting in a reduction in airflow speed. For example without the shroud choke, flow speeds in excess of 200 m s^{-1} could occur in the shroud during flight. However, with the choke point, flow speeds in the shroud during flight did not exceed 21 m s^{-1} during OMO-Asia 2015, which is sufficiently below the sample velocities of IPI during flight ($44\text{--}53\text{ m s}^{-1}$). Additionally, it limits non-parallel flows across the IPI nozzle created by variable pitch, roll, and yaw changes of the aircraft. As the aircraft changes pitch, roll, and yaw, the measured OH variability increases by $\pm 4.51 \times 10^4\text{ cm}^{-3}$ (1σ), which is only 10 % to 15 % higher than the natural variability of OH. This increase in variability is negligible as it represents, depending on internal pressure, 19 % to 30 % of the detection limit of the instrument. Both of these effects of the external shroud improve the measurement performance by reducing variable wall losses of HO_x at the IPI nozzle under flight conditions. The IPI system (with a nozzle orifice diameter of 6.5 mm) samples (51 to 230 sL min^{-1}) from the central airflow moving through the internal shroud. A critical orifice is located at the end of IPI in the center of the IPI cross section, which enables the HORUS instrument to sample (3 to 17 sL min^{-1}) from the central flow moving through IPI. This further reduces influences of wall loss within IPI on the overall measured signal in the cells. The removal of excess flow moving through IPI occurs via a perforated ring that surrounds the base of the critical orifice cone, evacuated by a blower.

As with other LIF-FAGE HO_x instruments, HORUS measures an off-resonance signal to discern the net OH fluorescence signal. This is achieved by successive cycling of the laser tuning from on-resonance (measuring the total signal of OH fluorescence and the signal originating from other fluorescence and electronic sources) to off-resonance (measuring all the above except the OH fluorescence). The HORUS instrument utilizes the $Q_1(2)$ transition $X^2\Pi_{3/2}(v''=0) \rightarrow A^2\Sigma^+(v'=0)$ (Freeman, 1958; Dieke and Crosswhite, 1962; Langhoff et al., 1982; Dorn et al., 1995; Holland et al., 1995; Mather et al., 1997). The net OH signal (S_{OH}) is the differ-

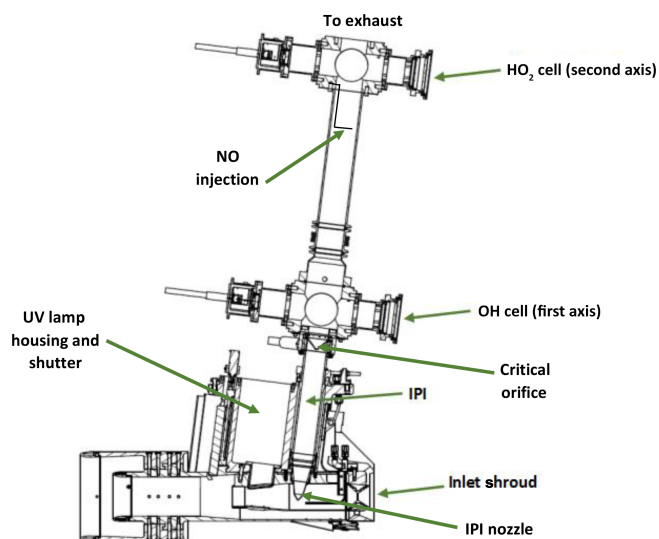


Figure 2. Overview of the airborne HORUS system as installed in the HALO aircraft. HO_2 is measured indirectly through the addition of NO that quantitatively converts HO_2 into OH. The NO injection occurs via a stainless-steel 1/8 in. (3.175 mm) line, shaped into a ring perpendicular to the airflow with several unidirectional apertures of 0.25 mm diameter creating essentially a NO shower.

ence between the on-resonance and off-resonance signals, OH-WAVE (Mao et al., 2012). The OH sensitivity (C_{OH}) and average laser power within the detection axis ($W_{z1\text{ pwr}}$) are then used to calculate the absolute OH mixing ratio (see Eq. 1). HO_2 is measured indirectly through the quantitative conversion of atmospheric HO_2 to OH by injection of nitric oxide (NO) under the low-pressure conditions within HORUS.



When NO is injected into the instrument, both ambient OH and HO_2 are measured in the second detection axis. The net HO_2 signal (S_{HO_2}) in the second axis is therefore derived from subtracting the net OH signal from the first detection axis normalized by the ratio of the OH sensitivities for the two detection axes ($C_{\text{OH}(2)}/C_{\text{OH}}$) from the net HO_x signal (S_{HO_x}). Then S_{HO_2} is corrected by the sensitivity to HO_2 (C_{HO_2}) and laser power ($W_{z2\text{ pwr}}$) to reach the absolute HO_2 mixing ratio (see Eq. 2).

$$[\text{OH}] = \frac{S_{\text{OH}}}{(C_{\text{OH}} \cdot W_{z1\text{ pwr}})}, \quad (1)$$

$$[\text{HO}_2] = \frac{1}{(C_{\text{HO}_2} \cdot W_{z2\text{ pwr}})} \cdot \left\{ S_{\text{HO}_x} - \frac{(C_{\text{OH}(2)} \cdot W_{z2\text{ pwr}})}{(C_{\text{OH}} \cdot W_{z1\text{ pwr}})} S_{\text{OH}} \right\}, \quad (2)$$

where $W_{z1\text{ pwr}}$ is the laser power in the first detection axis, $W_{z2\text{ pwr}}$ is the laser power in the second detection axis, and

C_{OH} and C_{HO_2} are the calibrated sensitivity factors for OH and HO_2 ($\text{cts s}^{-1} \text{ pptv}^{-1} \text{ mW}^{-1}$) respectively. By calibrating using a known OH mixing ratio, the instrument sensitivity C_{OH} can be determined by rearranging Eq. (1) to

$$C_{\text{OH(cal)}} = S_{\text{OH(cal)}} / ([\text{OH}] \cdot W_{z1 \text{ pwr}}). \quad (3)$$

The sensitivity of HORUS depends on the internal pressure, water vapor mixing ratios, and temperature, which are subject to change quite significantly during flight. Therefore, further parameterization when calibrating is required to fully constrain the sensitivity response of the instrument at various flight conditions. Equation (4) shows the terms that affect the sensitivity of the first HORUS axis that measures OH.

$$C_{\text{OH}}(P, T) = c_0 \cdot \rho_{\text{Int}}(P, T) \cdot Q_{\text{IF}}(P, T, \text{H}_2\text{O}) \cdot b_c(T) \cdot [\alpha_{\text{IPI}}(P, T) \cdot \alpha_{\text{HORUS}}(P, T)], \quad (4)$$

where c_0 is determined by calibrations and is the lump sum coefficient of all the pressure-independent factors affecting the HORUS sensitivity, for example, OH absorption cross section at 308 nm, the photon collection efficiency of the optical setup and quantum yield of the detectors, and pressure-independent wall loss effects. For calibrations, c_0 is normalized by laser power and has the units $\text{cts pptv}^{-1} \text{ s}^{-2} \text{ cm}^3 \text{ molecule}^{-1} \text{ mW}^{-1}$. ρ_{Int} is the internal molecular density. Q_{IF} is the quenching effect(s), which consists of the natural decay frequency of OH; OH decay due to collisional quenching that is dependent on pressure, temperature, and water vapor mixing ratio; and the detector opening and closing gating times after the initial excitation laser pulse. Both are pressure-dependent terms as denoted in Eq. (4). The Boltzmann correction (b_c) has a temperature dependency as it corrects for any OH molecules that enter the HORUS instrument in a thermally excited state and are therefore not measurable by fluorescence excitation at the wavelength used. α is the pressure-dependent OH transmission, which is the fraction of OH that reaches the point of detection. This term is separated for the two-tier pressure conditions present in the instrument. The term α_{IPI} represents the correction for pressure- and temperature-dependent OH loss on the walls within IPI. The term α_{HORUS} is the correction for pressure-dependent OH loss to the walls within the HORUS detection axes post critical orifice. While the quenching effects, internal densities, and Boltzmann corrections can be quantified by calculation, and the power entering the measurement cell is measured, the two factors that need to be determined through calibration are c_0 and OH transmission, α . Once the c_0 coefficient and α terms are known, the final in-flight-measured OH mixing ratio (pptv) is found:

$$[\text{OH}] = S_{\text{OH}} / (c_0 \cdot \rho_{\text{Int}} \cdot Q_{\text{IF}} \cdot b_c \cdot [\alpha_{\text{IPI}} \cdot \alpha_{\text{HORUS}}] \cdot W_{z1 \text{ pwr}}). \quad (5)$$

As S_{OH} scales with laser power, the terms that describe the instrument sensitivity shown as the denominator in Eq. (5), which ultimately have the units $\text{cts s}^{-1} \text{ pptv}^{-1} \text{ mW}^{-1}$, must

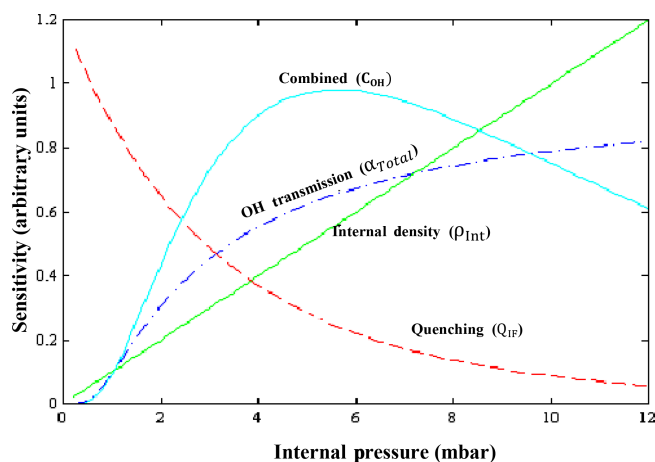


Figure 3. A schematic showing the overall sensitivity curve as a function of internal pressure (light blue line), OH transmission (dotted-dashed dark blue line), internal density (green line), and the quenching (dashed red line).

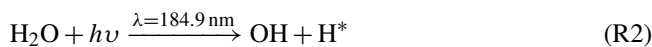
also be scaled to the measured laser power ($W_{z1 \text{ pwr}}$) during flight to acquire the absolute measurement of OH mixing ratio. As depicted in both Figs. 1b and 2, the complete system is calibrated with IPI attached and operating as it did when installed in the aircraft. Therefore, the combined losses of OH within IPI and in the low-pressure regime post critical orifice (that has a diameter of 1.4 mm) contribute to the overall calibrated C_{OH} sensitivity factor in the same way during measurement and calibrations, meaning that the OH transmission of HORUS can be quantified with both OH transmission terms (α_{IPI} and α_{HORUS}) combined into one term (α_{Total}).

$$[\text{OH}] = S_{\text{OH}} / (c_0 \cdot \rho_{\text{Int}} \cdot Q_{\text{IF}} \cdot b_c \cdot [\alpha_{\text{Total}}] \cdot W_{z1 \text{ pwr}}) \quad (6)$$

Figure 3 shows the schematic of the different factors described above and their impact on the overall sensitivity.

3 Calibration method and theory

As an overview, Table 1 shows common calibration techniques for OH instruments. The APACHE system is based on the production of known quantified and equal concentrations of OH and HO_2 via photolysis of water vapor in only synthetic air using a Hg ring lamp emitting UV radiation at 184.9 nm.



Stable water mixing ratios with a variability of $< 2\%$ were achieved by heating 300 sL min^{-1} flow of synthetic air to

353 K and introducing deionized water using a peristaltic pump into this heated gas flow, causing it to evaporate before entering a 15 L mixing chamber. This prevents recondensation and humidity spikes when the pump is introducing the water. The humidified gas flow is then diluted (to around 3 mmol mol^{-1}) and mixed further with additional dry pure synthetic air via a series of mixing blocks to achieve the required and desired stable water vapor mixing ratios. The photolysis of H_2O has only one spin-allowed and energetically viable dissociation channel at 184.9 nm (Engel et al., 1992), meaning the quantum yields of OH and H^* are unified (Sander et al., 2003). Even though Reaction (R3) is possible particularly since the H^* atoms can carry transitional energies of 0.7 eV at 189.4 nm (Zhang et al., 2000), the fast removal of energy by Reaction (R4) allows for the general assumption that all H^* atoms produced lead to HO_2 production (Fuchs et al., 2011). The use of water photolysis as a OH and HO_2 radical source for calibration of HO_x instruments has been adopted in a number of studies (Heard and Pilling, 2003; Ren et al., 2003; Faloon et al., 2004; Dusanter et al., 2008; Novelli et al., 2014; Mallik et al., 2018). As an example, the factors required to quantify the known concentrations of OH and HO_2 during calibrations are shown below:

$$[\text{OH}] = [\text{HO}_2] = [\text{H}_2\text{O}] \cdot \sigma_{\text{H}_2\text{O}} \cdot F_{184.9 \text{ nm}} \cdot \phi_{\text{H}_2\text{O}} \cdot t, \quad (7)$$

where in Eq. (7) the OH and HO_2 concentrations are a product of photolysis of a known concentration of water vapor $[\text{H}_2\text{O}]$, and $\sigma_{\text{H}_2\text{O}}$ is the absorption cross section of water vapor, $7.22(\pm 0.22) \times 10^{-20} \text{ cm}^2$ per molecule at 184.9 nm (Hofzumahaus et al., 1997; Creasey et al., 2000). $F_{184.9 \text{ nm}}$ is the actinic flux ($\text{photons cm}^{-2} \text{ s}^{-1}$) of the mercury lamp used for photolysis, $\phi_{\text{H}_2\text{O}}$ is the quantum yield, and t is exposure time. The quantum yield of water vapor photolysis at the 184.9 nm band is 1 (Creasey et al., 2000).

4 Results and discussion

4.1 Flow conditions

With any calibration device, the flow conditions must be characterized to inform subsequent methods and calibrations. Regarding APACHE, the two main factors to be resolved are (i) how uniform the flow speed profiles and therefore exposure times in respect to the APACHE cross section are and (ii) the impact of OH wall losses.

To this end, experimental and model tests were performed to determine whether the combination of the sintered filter as well as the stainless-steel perforated plates and wool arrangement could provide a homogeneous flow. This means that under operation the flow speeds should be uniform along the cross section of APACHE to within the uncertainty of the measurements. This is to ensure that the air masses passing across the lamp have the same exposure times irrespective

of where they are in the cross section. Additionally, model simulations can provide an indication of, as a function of APACHE pressure, the development and scale of boundary air conditions where air parcels experience extended contact time with the interior walls of APACHE and so have pronounced OH wall losses. This highlights potential flow conditions where there is sufficient time between the photolysis zone and the IPI nozzle to allow APACHE boundary air to expand into and influence the OH content of the air being sampled by HORUS.

4.1.1 Flow speed profiles

During calibration, the pressures within the HORUS instrument had to be controlled and monitored to replicate the in-flight conditions. The APACHE chamber pressure is equivalent to the in-flight pressure in the shroud where the HORUS system samples. The pressure of the detection axes depends on the pressure at the IPI nozzle and the efficiency of the pumps. Within IPI itself, the airflow through it is dependent on the pressure gradient between the shroud and the ambient pressure at the IPI exhaust or alternatively the APACHE pressure and pressure in front of the XDS35 scroll pump (post IPI blower). During the campaign, the exhausts of all blowers and pumps of the HORUS system were attached to the passive exhaust system of the aircraft and were thus exposed to ambient pressure. Therefore, the same IPI blower and pumps that were installed on HALO were used in the lab, and throughout the calibrations the pressure at the exhaust for every blower and pumps involved in the HORUS instrument was matched to the respective in-flight ambient pressures by attaching a separate pressure sensor, needle valve, and XDS35 scroll pump system. Additionally, to match the power that is provided on the aircraft, a three-phase mission power supply unit was used to power the pumps in the lab during testing and throughout the calibrations. Figure 4 shows the lab setup described above.

To limit the effect of wall loss, HORUS samples air from the core of the APACHE flow system and draws only a fraction of the total airflow as shown in Fig. 5. At 900 hPa the HORUS instrument takes 20 % and at 275 hPa HORUS takes 30 % of the total volume flow entering APACHE. To validate that this proportional volume flow into HORUS does not disturb the flow conditions within APACHE, flow speed profiles were performed using the Prandtl pitot tube installed directly opposite the IPI nozzle, which can be positioned flush against the internal wall up to 60.5 mm into the APACHE cavity, which is 15 mm from the APACHE center. Figure 6 shows the measured flow speed profile (blue data points) when the APACHE pressure was 920 hPa. As the distance between the APACHE wall and the pitot tube inlet increased, no significant change in the flow speed was observed. The largest change observed was between 46.6 and 60.5 mm where the flow speed increased by 0.16 m s^{-1} , which is 22.8 % smaller than the combined uncertainty of these two measurements

Table 1. Various known methods for OH instrument calibrations. CSTR stands for continuously stirred tank reactor.

	Technique	Method	Quoted (1σ) uncertainty	Limitations	References
(I)	Water UV photolysis	See Sects. 3 and 4	10 %–30 %	Dependent on lamp, photon flux measurement, and absorption	Creasey et al. (2003), Heard and Pilling (2003), Holland et al. (2003), Ren et al. (2003), Faloon et al. (2004), Smith et al. (2006), Martinez et al. (2010), Mallik et al. (2018)
(II)	Pulsed N ₂ –H ₂ O RF discharge	At low pressure (0.1 Torr); OH and NO produced using a low-power RF discharge. Concentrations of NO and OH are closely linked.	20 %	Requires NO measurement using stable ambient air calibrations	Dilecce et al. (2004), Verreycken and Bruggeman (2014)
(III)	Low-pressure flow-tube RF discharge	OH radical production by titration of H atoms with NO ₂ . Known amount of H atoms produced using microwave discharge using low-pressure flow tube.	30 %	Stable ambient air calibrations	Stevens et al. (1994)
(IV)	Continuously stirred tank reactor and decay of select hydrocarbons	In a CSTR, OH produced through UV irradiation of humidified airflow with injection of a specific hydrocarbon (1,3,5-trimethylbenzene, C ₉ H ₁₂) and NO. More recent studies have used cyclohexane, <i>n</i> -pentane and iso-butene. Concentrations of OH relate to decay rate of the hydrocarbon.	24 %–36 %	Time intensive, systematic wall loss of OH in reactor	Hard et al. (1995, 2002), Winiberg et al. (2015)
(V)	Steady-state O ₃ alkene	A steady-state OH concentration produced from ozonolysis of a known concentration of an alkene.	42 %	Time-consuming, large uncertainties compared to other methods	Heard and Pilling (2003), Dusanter et al., 2008)
(VI)	Laser photolysis of ozone	Photolysis of O ₃ with 284 nm light producing O(¹ D), which then reacts with H ₂ O producing OH.	40 %–50 %	Requires large apparatus	Tanner and Eisele (1995)

$\pm 0.21 \text{ m s}^{-1}$ (2σ). Compared to the other four measurement points performed at 920 mbar, the 1.54 m s^{-1} measured at 60.5 mm is not significantly different. However, when performing the speed profile tests at lower pressures, the pressure difference measured was close to or below the resolution of the differential pressure sensor. Consequently, the flow inside APACHE and the IPI nozzle was simulated using the computational fluid dynamics (CFD) model from COMSOL Multiphysics to gain a better understanding of the flow speed profiles at all pressures. The CFD module in COMSOL uses Reynolds-averaged Navier–Stokes (RANS) models (COM-

SOL, 2019). The standard *k*-epsilon turbulence model with incompressible flows was used for this study as it is applicable when investigating flow speeds below 115 m s^{-1} (COMSOL, 2019). An extra fine gridded mesh of a perforated plate with a high solidity ($\sigma_s = 0.96$) was implemented in the turbulence model to generate the turbulence and replicate the flows created by the bronze sintered filter (Roach, 1987). The model was constrained with the pressures measured within APACHE and IPI. The volume flow was calculated from the measured mass flow entering APACHE, and temperatures were constrained using the thermistor readings.

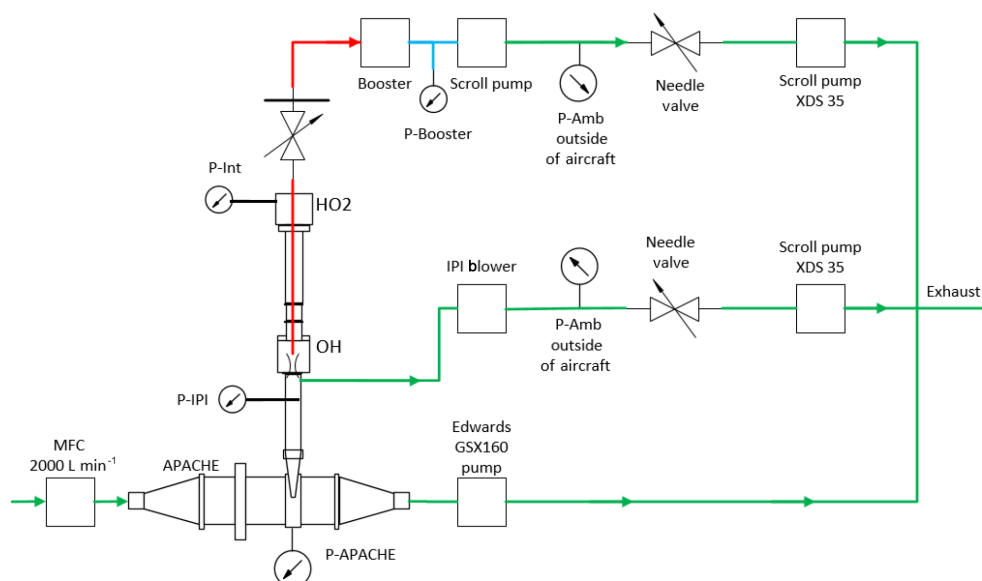


Figure 4. The experimental setup with the additional needle valves, pressure sensors, and XDS35 scroll pumps attached to the exhausts of all pumps and blowers of HORUS to match in-flight pumping efficiencies when calibrating with APACHE. The red lines depict the low-pressure region within HORUS, the blue is the pressure monitoring line between the booster and scroll pump that drive the HORUS sample flow, and the green shows the external gas lines.

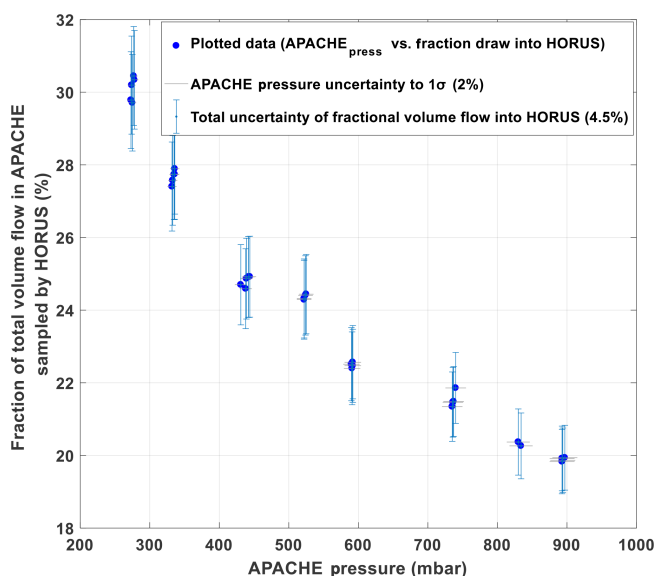


Figure 5. The percentage of the total volume flow entering APACHE, which is sampled by HORUS as a function of pressure within APACHE. All error bars are quoted to 1σ .

To gain confidence in the model, the flow speed output data were compared to the available measured flow speed profile (see Fig. 6).

Overall, the modeled flow speed profile did not differ significantly from that measured. The only point where the model significantly disagreed with measurements was at the boundary (< 4 mm away from the APACHE wall), where

the model predicted a flow speed of 1.3 m s^{-1} , which is 6 % lower than the minimum extent of the measurement uncertainty 1.38 m s^{-1} . This disagreement could also be due to the uncertainty in the parametrization of the boundary conditions in the COMSOL simulations. However, as this is occurring within a region that ultimately does not influence the air entering HORUS (see Sect. 4.1.2), the disagreement between modeled and measured flow speeds at distances less than 4 mm from the APACHE wall is ignored. Figure 7 shows the simulated flow speeds at six discrete pressures within APACHE.

The black lines depict the streamlines of the HORUS sample flow and the color gradient relates to the flow speed. The flow conditions in the center flow within the IPI nozzle, the center of the streamlines, and the undisturbed flow airflow not influenced by the sample flow of the HORUS instrument are indicated. The figure shows the internal APACHE dimensions starting from the sintered filter to the first perforated stainless-steel plate 0.135 and 0.601 m from the APACHE inlet, respectively. From the simulations, the centerline flow speed differs by less than 0.1 % compared to the undisturbed flow, which is also the case at 275 mbar when HORUS is drawing in the highest percentage of the total volume flow entering APACHE. After the sintered filter the high calculated Reynolds numbers ($Re > 2300$) support the statement that a turbulent flow regime is created. Additionally, the measurements in conjunction with simulations show that the small pores of the sintered filter release a uniform distribution of small turbulent elements across the diameter of

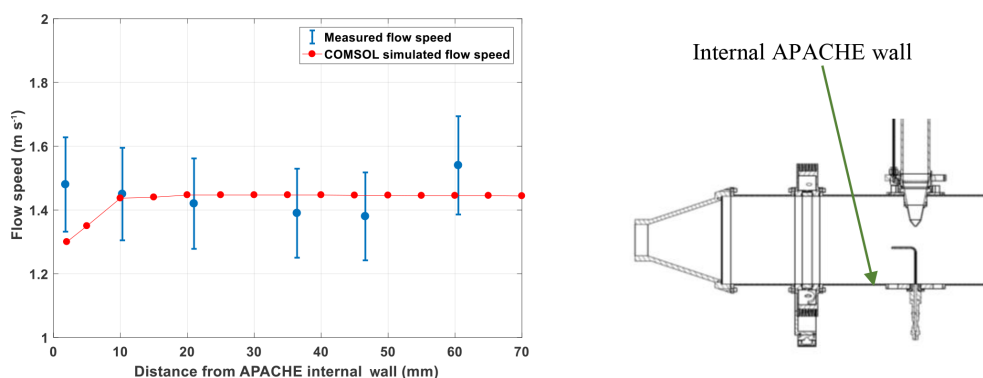


Figure 6. The measured (blue) and COMSOL simulated (red) flow speed profiles within APACHE, at 920 hPa. The x axis is the distance from the internal wall of APACHE. The error bars are quoted to 2σ .

APACHE, which remain prevalent all the way up to the IPI nozzle.

4.1.2 HO_x losses in APACHE

The modeled OH mixing ratios (pptv) in Fig. 8 show the change in OH content as the air flows along the length of APACHE. Mixing ratios were used as they are independent of the changing density within APACHE. In every simulation, the OH and HO₂ concentrations were initialized at zero, and losses at the walls were fixed to 100 % for both OH and HO₂. The radial photolytic production of OH and HO₂, as calculated using Eqs. (7) and (9), occurred when the air passed the UV ring lamp. For all simulations, the HO_x radical–radical recombination loss reactions (Reactions R6–R8) and the measured molecular diffusion coefficient of OH_{Dm} in air (Tang et al., 2014) were used:

$$\text{OH}_{\text{Dm}} = 179(\pm 20) \text{ Torr cm}^2 \text{ s}^{-1} \quad (239 \pm 27 \text{ hPa cm}^2 \text{ s}^{-1}).$$

In literature, there have been no reports of successfully performed tests that accurately measure HO₂ diffusivity coefficients in air. However, calculations of HO₂ diffusion coefficients using the Lennard-Jones potential model have been performed (Ivanov et al., 2007). Ivanov et al. (2007) performed a series of measurements and Lennard-Jones potential model calculations to quantify the polar analogue diffusion coefficients for OH, HO₂, and O₃ in both air and pure helium. The calculated OH and O₃ diffusion coefficients in air from the Lennard-Jones potential model were in good agreement with the recommended measurement values in Tang et al. (2014) and were well within the given uncertainties. Therefore, to best replicate the diffusivity of HO₂ within the simulations, the following diffusion coefficient of HO₂ in air from the Ivanov et al. (2007) paper was used:

$$\text{HO}_{2\text{Dm}} = 107.1 \text{ Torr cm}^2 \text{ s}^{-1} \quad (142.8 \text{ hPa cm}^2 \text{ s}^{-1}).$$

It is clear from Fig. 8 that irrespective of pressure the air masses at the boundary (where wall losses are 100 %) do not have sufficient time to expand into the HORUS sample flow streamlines and influence HO_x content entering HORUS. Lateral exchanges between air at the walls of APACHE and the free air in the center are suppressed due to the preservation of the small turbulence regime between the sintered filter and IPI. Table 2 provides, for six pressures, the evolution of OH along the length of APACHE, within the streamlines created by the HORUS sample flow as depicted in Fig. 8.

In Table 2, the L term represents OH mixing ratios on the leftmost HORUS sample flow streamline shown in Figs. 7 and 8. C represents OH mixing ratios in the center of the HORUS sample flow streamlines shown in Figs. 7 and 8. R represents OH mixing ratios on the rightmost HORUS sample flow streamline shown in Figs. 7 and 8. The mean mixing ratio at each APACHE pressure does not change significantly and is thus independent of the distance from the lamp. Conversely, the standard deviations of the OH mixing ratios within the HORUS sampling streamlines decrease as the distance from the lamp increases, indicating that the air is homogenizing. However, Fig. 8 and Table 2, with support from available measurements, indicate that the OH-depleted air masses (i.e., air masses that have experienced loss of OH on the APACHE walls) do not expand into and influence the OH content of air that is being sampled by HORUS. The main loss process that influences HO_x entering HORUS is the wall loss occurring at the IPI nozzle itself. According to the COMSOL simulations, around $22.2(\pm 0.8) \%$ (1σ) of OH and HO₂ is lost at the nozzle. This value does not significantly change with pressure, indicating that the HO_x loss at the nozzle is pressure independent. As described in Sect. 2.3, the pressure-independent sensitivity coefficients are a lump sum value containing the pressure-independent wall losses for OH and HO₂. Therefore, the characterized pressure-independent sensitivity coefficients, shown in Sect. 4.3, have the OH and HO₂ losses at the IPI nozzle constrained within them.

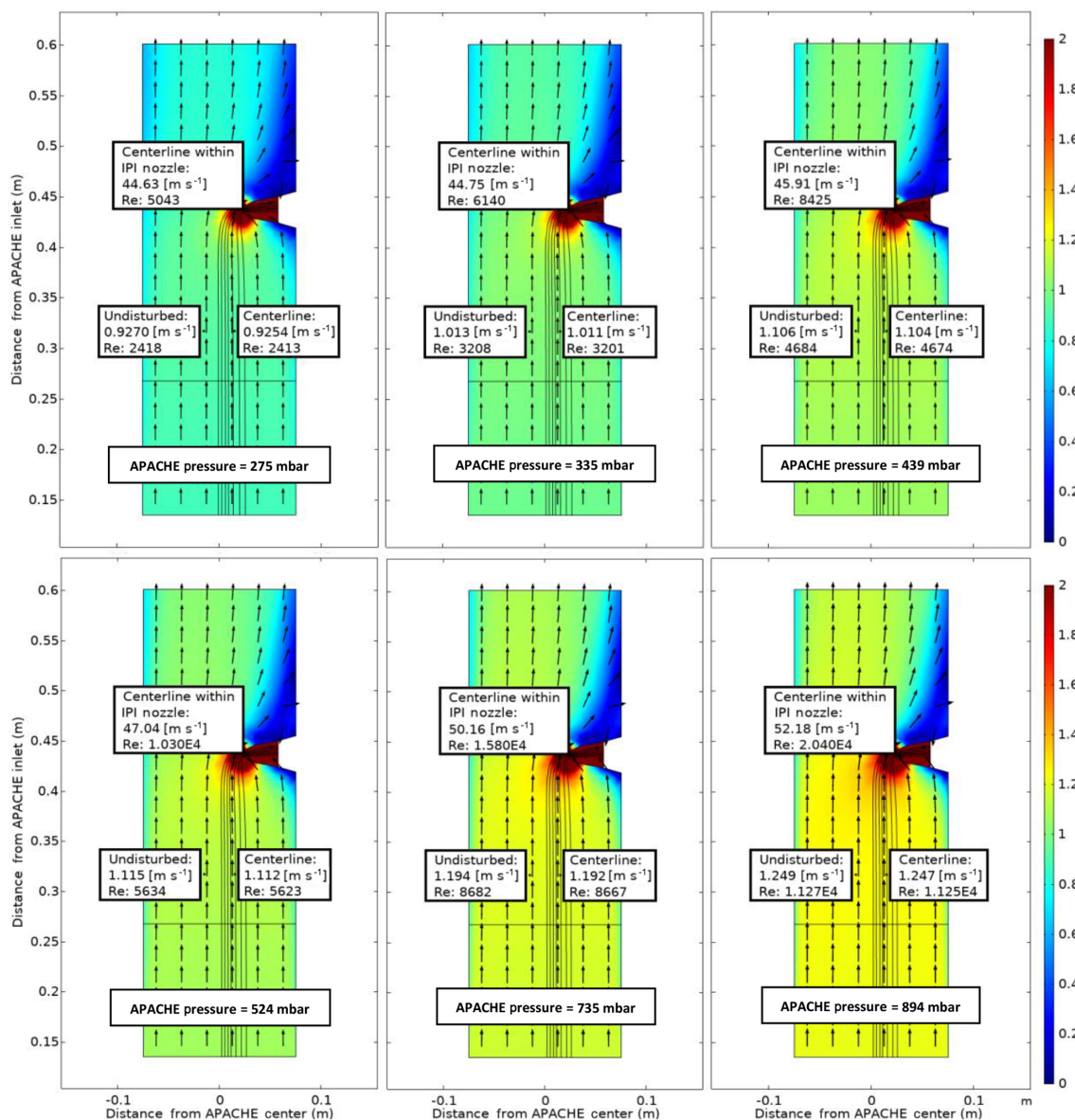


Figure 7. COMSOL Multiphysics output data, simulating the flow speed conditions at six discrete pressures within APACHE ranging from 275 to 894 mbar, between the sintered filter and the first perforated stainless-steel plate. The color represents flow speed in meters per second (m s^{-1}). The black lines are the streamlines created by the HORUS sample flow. The black arrows depict the flow direction. The x axis is the distance from the center of APACHE in meters. The y axis is the distance from the APACHE inlet. The “centerline within the IPI nozzle” labels show the flow conditions in the center of the fully formed flows after the HORUS pinhole, the “undisturbed” labels show the flow conditions outside of the HORUS streamlines, and the “centerline” labels show the flow conditions in the center of the streamlines (i.e., the area of flow influenced by HORUS sampling).

4.2 UV conditions

The photolysis lamp is housed in a mount with the side facing into the chamber having an anodized aluminum band with thirty 8 mm apertures installed between the lamp and a quartz wall. The housing was flushed with pure nitrogen to purge any O_2 present before the lamp was turned on. The nitrogen flushing was kept on continuously thereafter. After approximately 1 h, the lamp reached stable operation conditions; i.e.,

the relative flux emitted by the lamp as measured by a photometer (seen in Fig. 1b at the UVL (ultraviolet lamp) on the underside of the APACHE chamber) was constant. The flux (F_β) entering APACHE is not the same as the flux experienced by the molecules sampled by HORUS (F). Factors influencing the ratio between F_β and F are as follows: (i) absorption of light by O_2 , which is particularly important as O_2 has a strong absorption band at 184.9 nm and the O_2

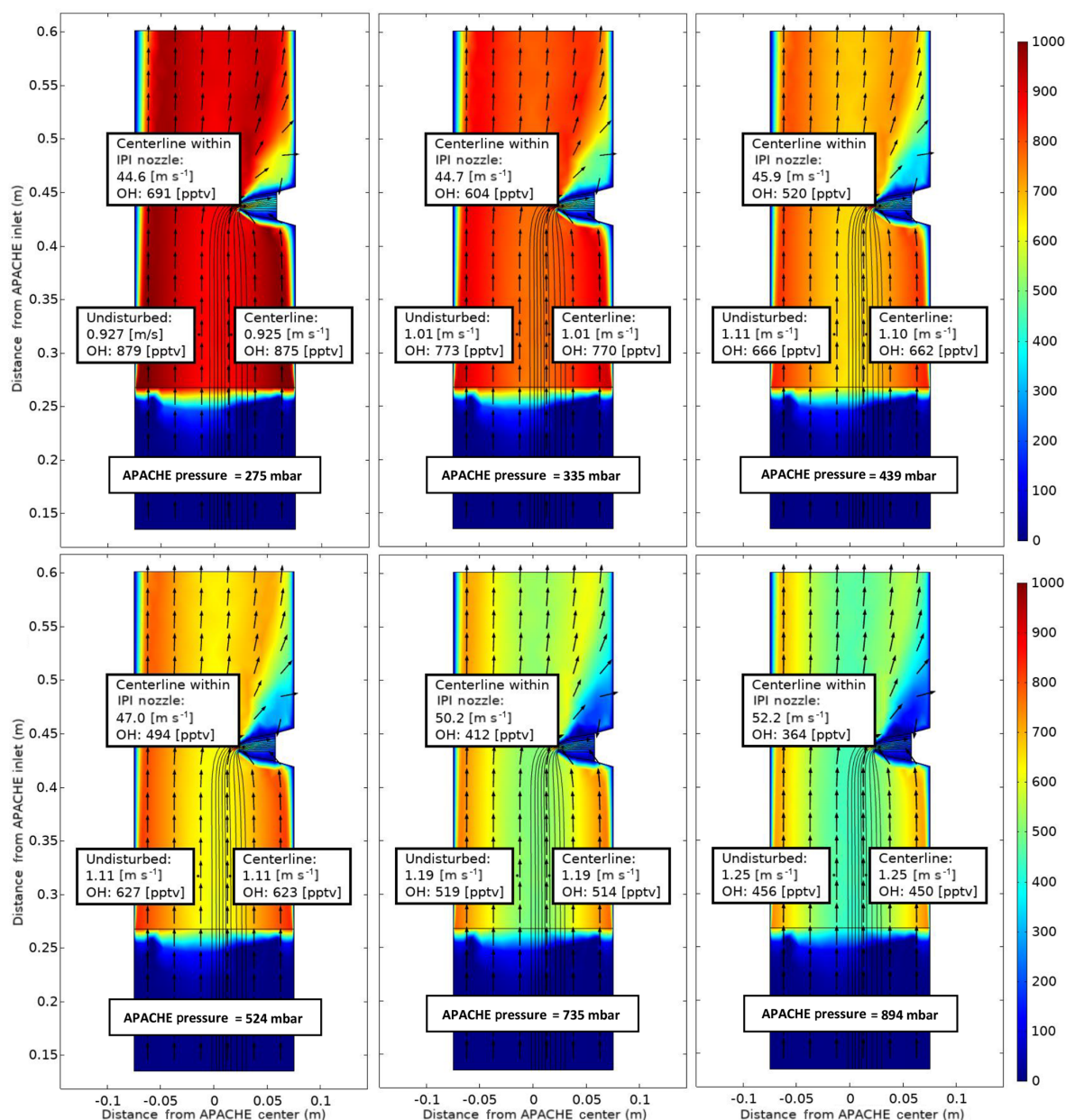


Figure 8. COMSOL Multiphysics output data, simulating OH conditions at six discrete pressures within APACHE ranging from 275 to 894 mbar, between the sintered filter and the first perforated stainless-steel plate. The color gradient is the OH mixing ratio (pptv), with initial OH production occurring at the lamp (0.26 m from APACHE inlet), using Eqs. (7) and (9), with water vapor mixing ratios kept constant at $3.2 \text{ mmol mol}^{-1}$. The black lines are the streamlines created by the HORUS sample flow. The black arrows depict the flow direction. The x axis is the distance from the center of APACHE in meters. The y axis is the distance from the APACHE inlet. The “centerline within IPI nozzle” labels represent the flow and OH concentrations in the center of the fully formed flows after the HORUS pinhole. The “undisturbed” labels show the flow conditions outside of the HORUS streamlines, and the “centerline” labels show the flow conditions in the center of the streamlines (i.e., influenced by HORUS sampling).

density changes in APACHE when calibrating at the different pressures; (ii) the variable radial flux, which is dependent on the geometric setup of the ring lamp and on the location within the irradiation cross section where the molecule is passing. These factors were resolved through the combination of two actinometrical cross-check methods. The advan-

tage of actinometrical methods is that the flux calculated is derived directly from the actual flux that is experienced by the molecules themselves as they pass through the APACHE chamber.

The first actinometrical method (A) used the HORUS instrument as a transfer standard to relate the flux of a precal-

Table 2. The evolution of OH within the HORUS sample flow streamlines, along the length of APACHE at all six pressures, within the streamlines created by HORUS sampling as depicted in Fig. 8. The *L* term represents OH mixing ratios on the left most streamline, *C* represents OH mixing ratios in the center of the streamlines, and *R* represents OH mixing ratios on the right most streamline. The centerline within IPI nozzle column shows the OH mixing ratios in the center of the flow in the HORUS inlet. All standard deviations are quoted to 1σ .

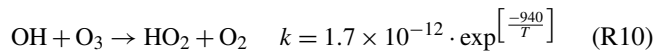
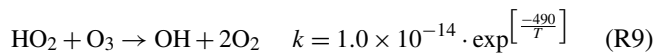
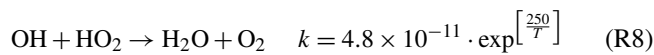
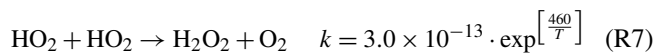
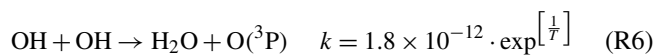
APACHE pressure (mbar)	OH (pptv) at lamp					OH (pptv) 4.2 cm from lamp					OH (pptv) 8.4 cm from lamp					OH (pptv) 12.8 cm from lamp					OH (pptv) 2 cm before HORUS inlet					In centerline within IPI nozzle (pptv)
	<i>L</i>	<i>C</i>	<i>R</i>	Mean	SD (1σ)	<i>L</i>	<i>C</i>	<i>R</i>	Mean	SD (1σ)	<i>L</i>	<i>C</i>	<i>R</i>	Mean	SD (1σ)	<i>L</i>	<i>C</i>	<i>R</i>	Mean	SD (1σ)	<i>L</i>	<i>C</i>	<i>R</i>	Mean	SD (1σ)	
894	438	445	513	465	41.4	442	446	507	465	36.4	438	455	500	464	32.0	442	456	501	466	30.8	445	457	490	464	23.3	364
755	502	508	572	527	38.8	506	509	567	527	34.4	502	519	560	527	29.8	507	519	562	529	28.9	509	521	550	527	21.1	412
524	611	617	672	633	33.6	615	619	668	634	29.5	613	627	660	633	24.1	617	628	664	636	24.6	619	629	651	633	16.4	493
439	652	657	706	672	29.8	656	659	702	672	25.7	654	666	698	673	22.7	657	667	699	674	21.9	660	669	686	672	13.2	520
335	760	765	805	777	24.7	764	766	801	777	20.8	762	773	799	778	19.0	766	774	803	781	19.5	768	776	788	777	10.1	603
275	866	871	907	881	22.4	870	872	907	883	20.8	869	879	904	884	18.0	873	880	905	886	16.8	875	882	889	882	7.0	689

ibrated Pen-Ray lamp used on the ground-based calibration device to F_β entering APACHE. This entailed first calibrating the HORUS instrument using a precharacterized ground-based calibration device (Martinez et al., 2010). The precalibrated Pen-Ray lamp flux (ϕ_0) is calculated from the measured NO concentrations that are produced by irradiating a known mixture of N_2O in a carrier gas:

$$\phi_0 = \frac{(k_a [\text{N}_2] [M] + k_b [\text{N}_2] + k_c [\text{N}_2\text{O}] + k_d [\text{N}_2\text{O}] [\text{NO}])}{2k_d [\text{N}_2\text{O}]^2 \sigma_{\text{N}_2\text{O}} f_{\text{N}_2\text{O}}}, \quad (8)$$

where $\sigma_{\text{N}_2\text{O}}$ is the absorption cross section of N_2O at 184.9 nm and $f_{\text{N}_2\text{O}}$ is the correction factor that accounts for the flux reduction via absorption by N_2O . A TEI NO monitor measures the NO concentration. For more details on how the ground calibration device is characterized using the photolysis of N_2O in conjunction with a TEI NO monitor, see Martinez et al. (2010). Since the precharacterized ground-based calibration device is designed to supply only 50 sL min^{-1} , and the sensitivity of the airborne HORUS instrument is optimized for high-altitude flying, the critical orifice diameter in HORUS was changed from the airborne configuration of 1.4 to a 0.8 mm on-ground* configuration. Additionally, the IPI system was switched to passive (i.e., the exhaust line from IPI to the IPI blower was capped). This was to adapt HORUS to a mass flow that the ground-based calibration device is able to provide and reduces the internal pressure within HORUS (from 18 to 3.5 mbar) to optimize the sensitivity towards OH at ambient ground level pressures (~ 1000 mbar). The asterisk discerns terms that were quantified when the smaller 0.8 mm critical orifice was used. The calculated instrument on-ground* sensitivity was then used to translate OH and HO_2 concentrations produced by the uv-technik Hg ring lamp into a value for F_β . Take note that for the direct calibrations of the airborne HORUS system using the characterized APACHE system, discussed in Sect. 4.3, the same initial 1.4 mm diameter critical orifice as used during the airborne campaign was installed. The HORUS on-ground* sensitivities at 1010 mbar for OH and HO_2 are $13.7(\pm 1.9)$ and $17.9(\pm 2.5) \text{ cts s}^{-1} \text{ pptv}^{-1} \text{ mW}^{-1}$ respectively, with the uncertainties quoted to 1σ . This sensitivity was then used to calculate the OH and HO_2 concentrations at the instrument nozzle with the APACHE system installed and operating at 1010 mbar. To ensure sufficient flow stability during calibration at this high pressure, the Edwards GSX160 scroll pump was disengaged. Additionally, the water mixing ratios were kept constant ($\sim 3.1 \text{ mmol mol}^{-1}$) and oxygen levels were varied by adding different pure N_2 and synthetic air mixtures, via MFCs. The OH and HO_2 concentrations at the IPI nozzle were $1.41(\pm 0.01)$ and $1.31(\pm 0.01) \times 10^{10} \text{ molecules cm}^{-3}$ respectively when using a water vapor mixing ratio of $3.1 \text{ mmol mol}^{-1}$ in synthetic air injected into APACHE. The uncertainties are quoted as measurement variability at 1σ . Using these values, the OH and HO_2 concentrations at the lamp were back calculated accounting for radical–radical loss Reactions (R6–R8) and HO_x reactions

with O₃ (Reactions R9–R10) using rate constants taken from Burkholder et al. (2015) with temperature (T) in Kelvin.



In APACHE when the Edwards GSX160 scroll pump was disengaged, the transit time between the UV radiation zone and the IPI nozzle was 0.18 s, resulting in chemical losses of 30 % to 33 % for OH and 27 % to 30 % HO₂, depending on oxygen concentration. Accounting for these chemical losses yields OH concentrations of $2.0(\pm 0.02) \times 10^{10}$ molecules cm⁻³ and HO₂ concentrations of $1.9(\pm 0.02) \times 10^{10}$ molecules cm⁻³ at the lamp, at 1010 mbar. The photon flux (F) experienced by the air sampled by HORUS, quantified using the OH and HO₂ concentrations stated above, ranged from 3.8×10^{14} to 6.7×10^{14} photons cm⁻² s⁻¹ depending on oxygen concentrations and considering the chemical losses. As described before, Eq. (7) shows how the production of OH at the lamp is calculated:

$$[\text{OH}] = [\text{H}_2\text{O}] \cdot \sigma_{\text{H}_2\text{O}} \cdot F_{184.9\text{ nm}} \cdot \phi_{\text{H}_2\text{O}} \cdot t. \quad (9)$$

$F_{184.9\text{ nm}}$ is the actinic flux encountered by the water molecules as they pass across the photolysis region, which is dependent on the attenuation of the flux (F_β) entering APACHE due to water vapor and O₂ molecules. Whereas the absorption coefficient of water vapor is constant across the linewidth of the 184.9 nm Hg emission line, the effective absorption cross section of molecular oxygen (σ_{O_2}) changes significantly at 184.9 nm within the linewidth of the Hg lamp (Creasey et al., 2000). Therefore, σ_{O_2} affecting the APACHE calibrations is dependent on O₂ concentration and the ring lamp temperature and current. Since the operating temperature of the uv-technik Hg lamp and the current applied (0.8 A) was kept constant during the actinometrical experiments and during the APACHE calibrations, any effect on σ_{O_2} regarding the ring lamp linewidth does not need to be investigated further in this study. The relationship of $F_{184.9\text{ nm}}$ to F_β can be derived using Beer–Lambert principles:

$$F_{184.9\text{ nm}} = F_\beta \cdot e^{-\left(\gamma_{\text{H}_2\text{O}}[\text{H}_2\text{O}] + \gamma_{\text{O}_2}[\text{O}_2]\right)}, \quad (10)$$

where F_β is the flux intensity entering APACHE from the ring lamp, with

$$\gamma_{\text{O}_2} = R_\beta \cdot \omega \cdot \sigma_{\text{O}_2}, \quad (11)$$

where R_β is the radial distance of the sampled air parcel to the ring lamp of APACHE; ω is a correction factor replicating

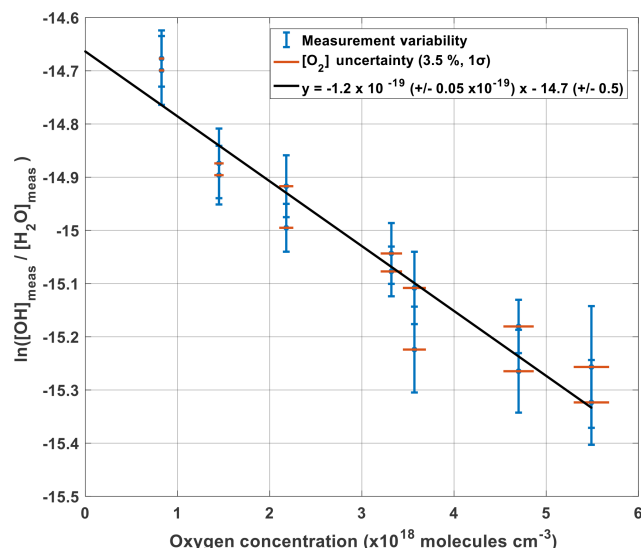


Figure 9. Plot showing the result of Eq. (11) as a function of oxygen concentration.

the integrated product of the absorption cross section and the ring lamp's emission line as modified by the effect of the absorption of O₂ present in between the lamp; and the flight path of the sampled air, normalized by σ_{O_2} , is the effective cross section of O₂. When combining Eqs. (7) and (9) the OH concentration produced at the lamp is quantified as

$$[\text{OH}] = [\text{H}_2\text{O}] \cdot \sigma_{\text{H}_2\text{O}} \cdot \phi_{\text{H}_2\text{O}} \cdot t \cdot F_\beta \cdot e^{-\left(\gamma_{\text{H}_2\text{O}}[\text{H}_2\text{O}] + \gamma_{\text{O}_2}[\text{O}_2]\right)}. \quad (12)$$

Equation (11) can be rearranged to

$$\ln\left[\frac{[\text{OH}]}{[\text{H}_2\text{O}]}\right] = \ln\left(F_\beta \cdot t \cdot \phi_{\text{H}_2\text{O}} \cdot \sigma_{\text{H}_2\text{O}}\right) + \left(-\gamma_{\text{H}_2\text{O}} \cdot [\text{H}_2\text{O}] - \gamma_{\text{O}_2} \cdot [\text{O}_2]\right). \quad (13)$$

Figure 9 shows the measured production of OH (left side of Eq. 12) plotted against oxygen concentration. Given that the other terms within Eq. (12) are constant with changing oxygen levels, the plotted gradient of the linear regression in Fig. 9 yields γ_{O_2} as a function of oxygen concentration being $1.2 \times 10^{-19}(\pm 0.05 \times 10^{-19})$ cm³ per molecule.

Given that the y intercept of the linear regression, -14.66, is equal to the natural logarithm of ($F_\beta t \phi_{\text{H}_2\text{O}}$) minus ($\gamma_{\text{H}_2\text{O}}[\text{H}_2\text{O}]$), the flux entering APACHE F_β can be characterized:

$$F_\beta = \left(\frac{e^{-14.66}}{t \cdot \phi_{\text{H}_2\text{O}}}\right) - (\gamma_{\text{H}_2\text{O}} \cdot [\text{H}_2\text{O}]) = 6.9 \times 10^{14}(\pm 1.1 \times 10^{14}) \text{ photons cm}^{-2} \text{ s}^{-1}. \quad (14)$$

The accuracy in F_β from method A is 15.9 % (1σ). Table 3 shows the parameters and their uncertainties contributing to the F_β characterized in method A.

Table 3. Parameters and uncertainties used in method A, using HORUS as a transfer standard. Overall uncertainty is the sum of the quadrature of the individual uncertainties. O(¹D) yield is taken from Martinez et al. (2010).

Parameter	Comments	Total uncertainty (1σ)
NO monitor (TEI)	Calibration uncertainty	5.2 %
NO standard (NPL)	Purity and concentration of the gas	1 %
N ₂ O cross section	JPL recommendation	2 %
H ₂ O cross section	JPL recommendation	2 %
γ _{O₂}	From method A	3.5 %
O(¹ D) yield	Martinez et al. (2010)	1 %
Kinetic rate coefficients	JPL recommendation	12 %
<i>F</i> _β variability	From method A	3.5 %
Photolysis chamber dimensions	Specifications of in-house workshop	3 %
[H ₂ O]	Calibration with NIST standard dew point generator	2 %
[O ₂]	From method A	3.4 %
Mass flow controllers	Calibration with NIST DryCal	2 %
Pressure and temperature sensors	Validated against NIST standard	2 %
Overall experimental stability	Variability of measured terms	4 %
Overall uncertainty		15.9 %

The second actinometrical method (B) involved using an ANSYCO O3 41 M ozone monitor to measure the ozone mixing ratio profile between the IPI nozzle and the wall surface of APACHE, at ground pressure (1021 mbar). This method utilizes O₂ photolysis at 184.9 nm, which produces two O(³P) atoms capable of reacting with a further two O₂ molecules to produce O₃.



The value of $1.2 \times 10^{-19} \text{ cm}^3$ per molecule for γ_{O₂} found in the previous method was used to calculate the actinic flux entering APACHE:

$$F_\beta = \frac{[\text{O}_3]}{[\text{O}_2] \cdot \gamma_{\text{O}_2} \cdot \phi_{\text{O}_2} \cdot t \cdot e^{-(\gamma_{\text{O}_2}[\text{O}_2]t)}} \quad (15)$$

Φ_{O₂} is the quantum yield of O₂ at 184.9 nm, which has been determined to be 1 between 242 and 175 nm (Atkinson et al., 2004). As in method A, the ozone produced at the lamp is quantified by back calculating from the ozone measured at the ANSYCO O3 41 M inlet position. Inside APACHE, typical ozone concentrations ranged from 1.26×10^{12} to $2.05 \times 10^{12} \text{ molecules cm}^{-3}$ depending on the oxygen concentration. From this approach, the calculated *F*_β is $6.11 \times 10^{14} (\pm 0.8 \times 10^{14}) \text{ photons cm}^{-2} \text{ s}^{-1}$ with a total uncertainty of 12.9 % (1σ). The final value taken for *F*_β is the average of the two experiments, weighted by their uncertainties:

$$\text{– actinic flux } (F_\beta) = 6.37 \times 10^{14} (\pm 1.3 \times 10^{14}) \text{ photons cm}^{-2} \text{ s}^{-1}$$

$$\text{– accuracy in } F_\beta = 20.5 \% (1\sigma)$$

– agreement for *F*_β between method A and B, zeta score = 0.59.

Table 4 shows the parameters and their uncertainties which contribute to the *F*_β characterized in method B.

4.3 Evaluation of instrumental sensitivity

Figure 10 shows the sensitivity curve of HORUS; the quenching effect; the linear fits used to quantify the pressure-independent sensitivity coefficients; and relative HO_x transmission values for OH, OH in the second axis, and HO₂ plotted as a function of the HORUS internal density. The red smoothed line in Fig. 10a represents the calculated sensitivity curve for each measurement using Eq. (4) and the characterized variables therein. Given that this calculated sensitivity curve for each measurement agrees to within 2σ of the uncertainties in measured calibration curves, we are confident that each of the terms described in Eq. (4) has been sufficiently resolved. Table 5 shows the ranges, precision, and uncertainties of measured or calculated variables affecting OH and HO₂ concentrations formed in APACHE.

The pressure-independent sensitivity coefficients (cN) for OH in the first axis (c0), OH in the second axis (c1), and HO₂ in the second axis (c2) are calculated by rearranging Eq. (4) to

$$c0 \cdot \rho_{\text{Int}}(P, T) = \frac{C_{\text{OH}}(P, T)}{Q_{\text{IF}}(P, T) \cdot b_c(T) \cdot [\alpha_{\text{IPI OH}}(P, T) \cdot \alpha_{\text{HORUS OH}}(P, T)]}, \quad (16)$$

$$c1 \cdot \rho_{\text{Int}}(P, T) = \frac{C_{\text{OH}(2)}(P, T)}{Q_{\text{IF}(2)}(P, T) \cdot b_c(T) \cdot [\alpha_{\text{IPI OH}}(P, T) \cdot \alpha_{\text{HORUS OH}(2)}(P, T)]}, \quad (17)$$

Table 4. Parameters and uncertainties involved in method B, using the ANSYCO O3 41 M monitor. The total uncertainty is the sum of the quadrature of the individual uncertainties.

Parameter	Comments	Total uncertainty (1σ)
O ₃ calibrator	Calibrated against a primary standard	2 %
[O ₃]	Calibration of ANSYCO O3 41 M monitor	4 %
[O ₂]	From method A	3.4 %
γ_{O_2}	From method A	3.5 %
F_β variability	From method A	3.5 %
Mass flow controllers	Calibration with NIST DryCal	2 %
Pressure and temperature sensors	Validated against NIST standard	2 %
Experimental stability	Variability of values	10.1 %
Overall uncertainty		12.9 %

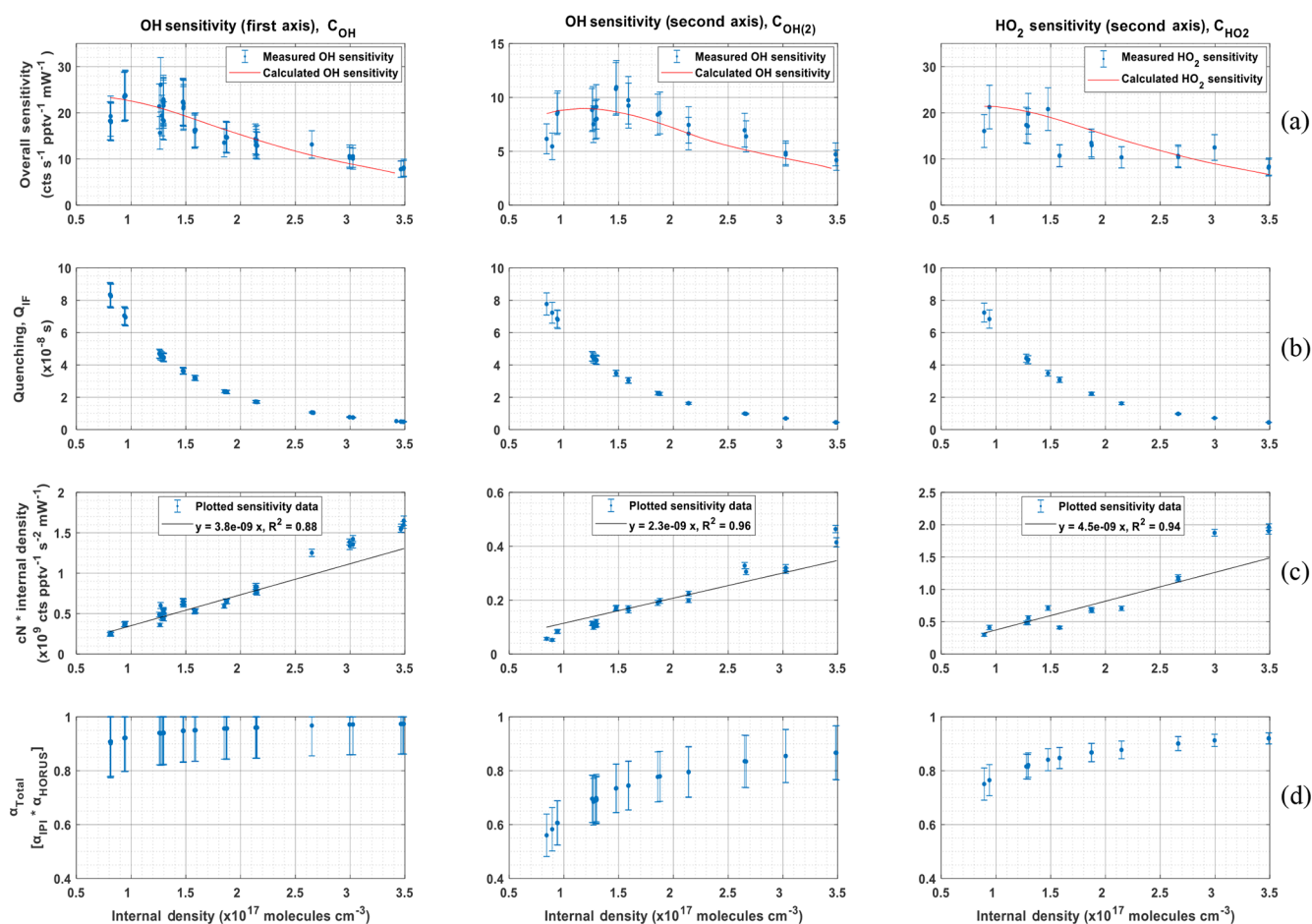
**Figure 10.** The determination of the pressure-based sensitivity of OH in both axes and HO_2 for HORUS. The data shown are 1 h averages for the tested pressures, all plotted with the internal density on the x axis. Row (a) is the measured (blue data points) HORUS sensitivity curve and calculated (red line) sensitivity curve. Row (b) is internal quenching by N_2 , O_2 , and water vapor. Row (c) is internal density and the pressure-independent sensitivity coefficient ($c\text{N}$; c_0 for the OH first axis, c_1 for OH second axis, and c_2 for HO_2). Row (d) is the total OH and HO_2 transmissions, all plotted against internal density. The error bars represent measurement variability (1σ) for rows (b, c). In rows (a, d), the error bars represent the total uncertainty (1σ).

Table 5. Parameters within APACHE, their ranges, and uncertainties, contributing to the uncertainty in the three measurement sensitivities within HORUS.

Parameter (unit)	Range or typical value	Precision (1 σ)	Total uncertainty (1 σ)
F_β at 184.9 nm (photons cm ⁻² s ⁻¹)	6.37×10^{14}	3.5 %	20.5 %
$\sigma_{\text{H}_2\text{O}}$ (cm ² per molecule)	7.22×10^{-20}	–	2 %
γ_{O_2} (cm ³ per molecule)	1.22×10^{-19}	1.8 %	3.5 %
$[\text{O}_2]$ ($\times 10^{18}$ molecules cm ⁻³)	1.1–4.8	1.4 %	3.4 %
$[\text{H}_2\text{O}]$ ($\times 10^{16}$ molecules cm ⁻³)	2.00–7.41	1.2 %	2 %
Mass flow controller (sL min ⁻¹)	203–988	< 2 %	2 %
Pressure sensors (mbar)	275–900	< 1 %	2 %
Temperature sensors (K)	282–302	< 1 %	2 %
Overall		5 %	21.5 %

$$c2 \cdot \rho_{\text{Int}}(P, T) = \frac{C_{\text{HO}_2}(P, T)}{Q_{\text{IF}(2)}(P, T) \cdot b_c(T) \cdot [\alpha_{\text{IPIHO}_2}(P, T) \cdot \alpha_{\text{HORUSHO}_2}(P, T)]}. \quad (18)$$

The products of Eq. (15) to (17) are plotted against internal density in Fig. 10c, where the slopes of the linear regressions are the pressure-independent sensitivity coefficients. Note that in Eqs. (16) and (17) the two bracketed terms are in relation to the OH measurement at the second axis. Table 6 shows the values, precision, and uncertainty in the quantified pressure-independent sensitivity coefficients.

In Fig. 10c the quenching (Q_{IF}) is plotted against internal density. Q_{IF} is calculated using the same approach as described in Faloon et al. (2004) and Martinez et al. (2010):

$$Q_{\text{IF}}(P) = \frac{1}{\Gamma} (e^{-\Gamma g_1} - e^{-\Gamma g_2}), \quad (19)$$

where Γ is the excited state decay frequency (Hz), consisting of the natural decay frequency, and decay due to collisional quenching that is dependent on pressure, temperature, and water vapor mixing ratio. g_1 and g_2 are the detector gate opening and closing times after the initial excitation laser pulse, which are set to 104 and 600 ns respectively.

As described in Sect. 2.3, the pressure-independent sensitivity coefficients are lump sum variables containing pressure-independent HO_x wall loss. The pressure-dependent HO_x transmission through the HORUS instrument is quantified and described below. In flight, IPI operates across the pressure range of 180 to 1010 mbar. However, within HORUS, post critical orifice, at detection axes where HO_x is measured the pressure ranges from 3.1 to 18.4 mbar. Therefore, the transmission through IPI (α_{IPI}) and through HORUS (α_{HORUS}) must be quantified separately using the corresponding measured pressures and transit times, before being combined as the total transmission ($\alpha_{\text{IPI}} \cdot \alpha_{\text{HORUS}} = \alpha_{\text{Total}}$). To calculate the transmission of HO_x within IPI, the following was used:

$$\alpha_{\text{IPIOH}} = 1 - \left[\frac{\text{OH}_{\text{DM}}(P) \cdot t_{\text{IPI}}(P, T) \cdot \pi}{\text{IPI}_A \cdot P_{\text{IPI}}} \right], \quad (20)$$

$$\alpha_{\text{IPIHO}_2} = 1 - \left[\frac{\text{HO}_{2\text{DM}}(P) \cdot t_{\text{IPI}}(P, T) \cdot \pi}{\text{IPI}_A \cdot P_{\text{IPI}}} \right], \quad (21)$$

where t_{IPI} is the transit time within IPI, i.e., the time it takes for air to flow from the IPI nozzle to the critical orifice of HORUS. IPI_A is the internal cross-sectional area of IPI and P_{IPI} is the measured pressure within IPI. The OH_{DM} and $\text{HO}_{2\text{DM}}$ terms are the OH and HO_2 diffusion coefficients as described in Sect. 4.1.2. α_{IPIOH} is the transmission of OH through IPI, and α_{IPIHO_2} is the transmission of HO_2 through IPI. By applying Eqs. (19) and (20), α_{IPIOH} and α_{IPIHO_2} ranged from 0.97 to 0.99 and 0.99 to 0.997 respectively across the pressure range within IPI of 198–808 mbar and IPI transit times of 90–120 ms. However, to calculate α_{Total} , the OH and HO_2 transmission post critical orifice, α_{HORUSOH} and $\alpha_{\text{HORUSHO}_2}$, must be resolved. α_{HORUS} regarding OH and HO_2 can be calculated by adapting Eqs. (19) and (20) to the internal HORUS conditions producing:

$$\alpha_{\text{HORUSOH}} = 1 - \left[\frac{\text{OH}_{\text{DM}}(P) \cdot t_{\text{r1}}(P, T) \cdot \pi}{\text{HORUS}_A \cdot P_{\text{int}}} \right], \quad (22)$$

$$\alpha_{\text{HORUSOH}(2)} = 1 - \left[\frac{\text{OH}_{\text{DM}}(P) \cdot t_{\text{r2}}(P, T) \cdot \pi}{\text{HORUS}_A \cdot P_{\text{int}}} \right], \quad (23)$$

$$\alpha_{\text{HORUSHO}_2} = 1 - \left[\frac{\text{HO}_{2\text{DM}}(P) \cdot t_{\text{r2}}(P, T) \cdot \pi}{\text{HORUS}_A \cdot P_{\text{int}}} \right], \quad (24)$$

where t_{r1} and t_{r2} are the transit times within HORUS from the critical orifice to the first and second detection axis respectively. HORUS_A is the internal cross-sectional area of HORUS, and P_{int} is the measured internal pressure within HORUS. The OH transmission from the critical orifice to the first detection cell (α_{HORUSOH}) ranged from 0.93 to 0.98, the OH transmission from the critical orifice to the second detection cell ($\alpha_{\text{HORUSOH}(2)}$) ranged from 0.58 to 0.87, and the HO_2 transmission from the critical orifice to the second detection cell ($\alpha_{\text{HORUSHO}_2}$) ranged from 0.76 to 0.92. These ranges are quoted under the HORUS internal pressure range of 3.7 to 13.7 mbar and internal transit times to the first detection axis (3.8 to 4.3 ms) and second detection axis (23.5

Table 6. Pressure-independent sensitivities and their overall uncertainty from calibrations with APACHE.

Parameter (cts pptv ⁻¹ s ⁻² cm ³ molecule ⁻¹ mW ⁻¹)	Value (× 10 ⁻⁹)	Precision (± 1σ)	Total uncertainty (1σ)
c0 for OH in OH axis	3.8	4 %	6.9 %
c1 for OH in HO ₂ axis	2.3	4 %	6.9 %
c2 for HO ₂ in HO ₂ axis	4.5	2 %	5.6 %

to 27.8 ms). The combined α_{Total} values for OH, OH at the second detection axis, and HO₂ are plotted in Fig. 10d as a function of the internal density of HORUS. Table 7 shows the calculated α_{Total} transmission terms; their precision; and uncertainty for OH to the first axis, OH to the second axis, and HO₂ to the second axis.

Table 8 shows the measured sensitivity values using APACHE for OH at the first axis (C_{OH}), OH at the second axis ($C_{\text{OH}(2)}$), and HO₂ at the second axis (C_{HO_2}). The precision denotes the 1σ variability in the measured HO_x signals from HORUS; the total uncertainty is the root sum square of the total uncertainty values from the variables listed in Tables 5 and 6.

The undescribed remaining fraction that influences the instrument sensitivity ($R_{\text{undescribed}}$) is calculated by dividing the overall sensitivity values described in Eq. (4):

$$R_{\text{OH}} = \frac{C_{\text{OH}}}{c0 \cdot \rho_{\text{int}}(P, T) \cdot Q_{\text{IF}}(P, T) \cdot b_c(T) \cdot [\alpha_{\text{IPI OH}}(P, T) \cdot \alpha_{\text{HORUS OH}}(P, T)]}, \quad (25)$$

$$R_{\text{OH}(2)} = \frac{C_{\text{OH}(2)}}{c1 \cdot \rho_{\text{int}}(P, T) \cdot Q_{\text{IF}(2)}(P, T) \cdot b_c(T) \cdot [\alpha_{\text{IPI OH}}(P, T) \cdot \alpha_{\text{HORUS OH}(2)}(P, T)]}, \quad (26)$$

$$R_{\text{HO}_2} = \frac{C_{\text{HO}_2}}{c2 \cdot \rho_{\text{int}}(P, T) \cdot Q_{\text{IF}(2)}(P, T) \cdot b_c(T) \cdot [\alpha_{\text{IPI HO}_2}(P, T) \cdot \alpha_{\text{HORUS HO}_2}(P, T)]}, \quad (27)$$

$$R_{\text{undescribed}} = \{R_{\text{OH}}; R_{\text{OH}(2)}; R_{\text{HO}_2}\},$$

where $R_{\text{undescribed}}$ is a matrix containing the undescribed remaining factors from the three measurements. When plotting $R_{\text{undescribed}}$ against the internal pressure of HORUS, (see Fig. S10), the data scatters $\pm 0.15(1\sigma)$ about the average value of $1.02 (\pm 0.23, 1\sigma \text{ calibration uncertainty})$. This means that (as an upper limit) $< 2\%$ of the overall instrument sensitivity is unresolved by the terms described in Eq. (4). Additionally, the 1σ variability of the $R_{\text{undescribed}}$ is 34 % smaller than the uncertainty in the APACHE calibration, meaning that this remaining fraction is declared as neither pressure dependent nor pressure independent.

It is important to note here that all data shown in Fig. 10, with the exception of the pressure-independent sensitivity coefficients, are in relation to temperatures and pressures HORUS experienced during calibrations in the lab. To apply these findings to real airborne measurements, the pressure- and temperature-dependent terms in Eq. (4) are calculated using the temperatures and pressures that are measured

within the instrument during flight. The only terms that affect measurement sensitivity and are directly transferable from the calibrations with APACHE to the measurements in flight shown in Eq. (4) are the pressure-independent sensitivity coefficient as they are not subject to change with the large temperature and pressures ranges HORUS experiences when airborne. Figure 11 shows the pressure- and temperature-dependent terms from Eq. (4) characterized for a typical flight that took place during the OMO-Asia 2015 airborne campaign. In Fig. 11, the sensitivity values, limit of detection, transmission values for OH (blue data points) and HO₂ (red data points), and the ambient water mixing ratios (black data points) that occurred during flight 23 are plotted as a function of altitude. During flight, the OH sensitivity ranged from $5.4(\pm 1.2) \text{ cts s}^{-1} \text{ pptv}^{-1} \text{ mW}^{-1}$ on the ground to $24.1(\pm 5.4) \text{ cts s}^{-1} \text{ pptv}^{-1} \text{ mW}^{-1}$ at 14 km. The HORUS sensitivity values for HO₂ ranged from $5.5(\pm 1.2) \text{ cts s}^{-1} \text{ pptv}^{-1} \text{ mW}^{-1}$ and reached an average maxima of $20.5(\pm 4.5) \text{ cts s}^{-1} \text{ pptv}^{-1} \text{ mW}^{-1}$ at 11.4 km. Above 11.4 km the HO₂ sensitivity decreased with altitude, reaching $19.7(\pm 4.4) \text{ cts s}^{-1} \text{ pptv}^{-1} \text{ mW}^{-1}$ at 14 km. This drop in HO₂ sensitivity is attributable to the increasing decline in HO₂ transmission inside HORUS as the aircraft flies higher, despite the sensitivity improvements via quenching as the air is becoming drier. The water vapor mixing ratios at 14 km on average are 3 orders of magnitude lower than the average water vapor mixing ratio of 1.5 % at ground level, which greatly suppresses quenching of OH and thus is the main driver for the general increasing trend in the instrument sensitivity towards HO_x as altitude increases. Additionally, Fig. 11 shows that the limit of detection for both OH and HO₂ decrease with increasing altitude. For OH, the HORUS limit of detection is $\sim 0.11 \text{ pptv}$ at ground level and drops to $\sim 0.02 \text{ pptv}$ at 14 km. For HO₂ the limit of detection is $\sim 1.2 \text{ pptv}$ at ground level and drops to 0.23 pptv at 14 km.

5 Conclusions

The overall goal of this study was to develop and test a new calibration system capable of providing the high flows required by the airborne HORUS system while maintaining stable pressures across the pressure ranges experienced during flight. Such systems are critical to suitably characterize airborne systems (such as a LIF-FAGE measuring HO_x) that have a strong pressure-dependent sensitivity. In addition, this

Table 7. Pressure-dependent OH and HO₂ transmission and their overall uncertainty from calibrations with APACHE.

Parameter (%)	Value	Precision ($\pm 1\sigma$)	Total uncertainty (1σ)
α_{Total} (for OH to OH axis)	90–97	2.8 %	14.3 %–11.5 %
α_{Total} (for OH to HO ₂ axis)	56–86	4.3 %	14.1 %–11.5 %
α_{Total} (for HO ₂ to HO ₂ axis)	75–92	2.9 %	7.9 %–2.2 %

Table 8. Pressure-dependent sensitivities for the three measurement within HORUS and their overall uncertainty from calibrations with APACHE. The range in the precision relates to the numbers quoted in the value column.

Parameter (unit)	Value	Precision ($\pm 1\sigma$)	Total uncertainty (1σ)
C_{OH} (cts s ⁻¹ pptv ⁻¹ mW ⁻¹)	7.8–26.1	1.1 %–0.5 %	22.6 %
$C_{\text{OH}(2)}$ (cts s ⁻¹ pptv ⁻¹ mW ⁻¹)	4.2–11.0	2.0 %–0.3 %	22.6 %
C_{HO_2} (cts s ⁻¹ pptv ⁻¹ mW ⁻¹)	8.1–21.2	0.4 %–0.7 %	22.2 %

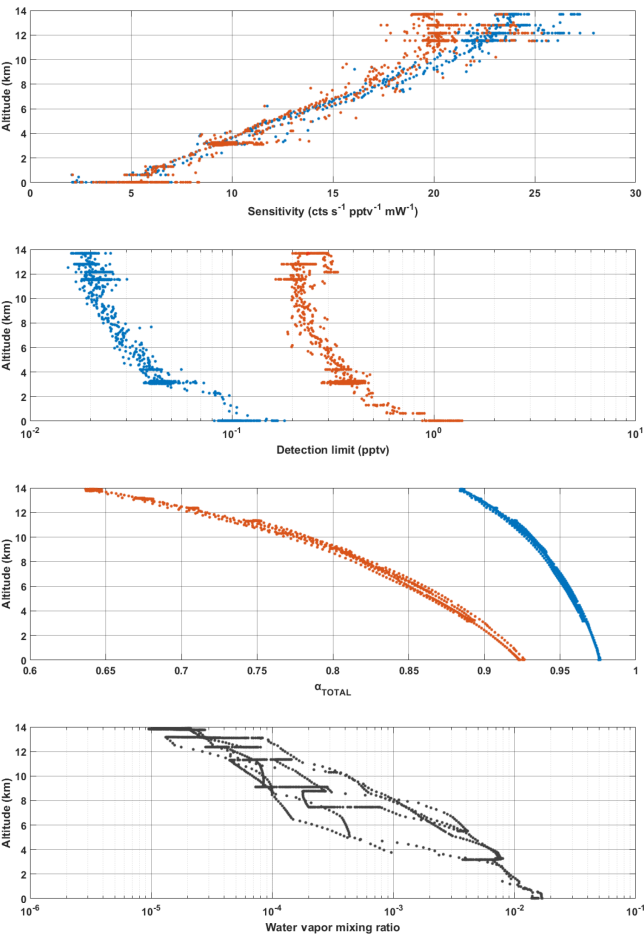


Figure 11. In-flight sensitivity curves, limit of detection, and HO_x transmission plotted against altitude for OH (blue data points) and HO₂ (red data points), and the water vapor mixing ratio (black data points) plotted against altitude in kilometers (bottom plot). Data taken from flight 23.

system is purely based on the use of water vapor photolysis, which is a frequently adopted technique for HO_x instrument calibration (Martinez et al., 2003; Faloona et al., 2004; Dusanter et al., 2008). The COMSOL Multiphysics simulations constrained by temperature, pressure, and mass flow measurements demonstrated that air masses at the boundary of the APACHE system do not have sufficient time to expand into the streamlines created by the HORUS sample flow and influence the HO_x content entering HORUS. The largest uncertainties result from constraining the flux (F_{β}) entering APACHE ($6.37 \pm 1.3 \times 10^{14}$ photons cm⁻² s⁻¹, 1σ) and the total uncertainty in the pressure-independent sensitivity coefficients (ranging from 5.6 % to 6.9 %, 1σ). The two actinometrical methods used to derive F_{β} proved to be in good agreement with a zeta score of 0.59, considering 1σ of their uncertainties. The HORUS transfer standard method yielded an F_{β} value of $6.9 \pm 1.1 \times 10^{14}$ photons cm⁻² s⁻¹ (1σ), and the ozone monitor method yielded an F_{β} value of $6.11 \pm 0.8 \times 10^{14}$ photons cm⁻² s⁻¹ (1σ). Furthermore, the APACHE system enabled the total OH and HO₂ pressure-dependent transmission factors to be characterized as a function of internal pressure. Calculations of HO_x diffusivity to the walls within IPI and the low-pressure regime within HORUS yielded 90 %–97 % for OH transmission to the first detection axis, 56 %–86 % for OH transmission to the second detection axis, and 75 %–92 % for HO₂ transmission to the second detection axis. Future studies with APACHE are planned to expand upon the findings within this paper, with a particular focus on temperature control and on improving operational pressure and flow speed ranges. However, in this study, the APACHE calibration system has demonstrated that, within the lab, it is sufficiently capable of calibrating the airborne HORUS instrument across the pressure ranges the instrument had experienced in flight during the OMO-Asia 2015 airborne campaign. The overall uncertainty of 22.1 %–22.6 % (1σ) demonstrates that this calibration approach with APACHE compares well with other

calibration methods described earlier in Table 1. Nevertheless, there is potential for improvement. Accurate calibrations of instruments, particularly airborne instruments that have strong pressure-dependent sensitivities, are critical to acquiring concentrations of atmospheric species with minimal uncertainties. Only through calibrations can the accuracy of measurements be characterized and allow for robust comparisons with other measurements and with models to expand our current understanding of chemistry that occurs within our atmosphere.

Data availability. The research dataset is fully and openly accessible via <https://doi.org/10.5281/zenodo.3821976> (Marno and Harder, 2020).

Supplement. The supplement related to this article is available online at: <https://doi.org/10.5194/amt-13-2711-2020-supplement>.

Author contributions. KH, CE, MM, HH, UJ, and MR formulated the original concept and designed the APACHE system. DM, HH, and UJ prototyped, developed, and characterized the APACHE system. TK, DM, and HH developed and performed the CFD simulations. DM prepared the manuscript with contributions from all coauthors.

Competing interests. The authors declare that they have no conflict of interest.

Acknowledgements. We would like to take this opportunity to give a thank you to the in-house workshop at the Max Planck Institute for Chemistry for construction and guidance in the development of APACHE. Additionally, we would like to extend a special thank you to Dieter Scharffe for his assistance and advice during the development stage of this project.

Financial support. The article processing charges for this open-access publication were covered by the Max Planck Society.

Review statement. This paper was edited by Lisa Whalley and reviewed by two anonymous referees.

References

Albrecht, S. R., Novelli, A., Hofzumahaus, A., Kang, S., Baker, Y., Mentel, T., Wahner, A., and Fuchs, H.: Measurements of hydroperoxy radicals (HO_2) at atmospheric concentrations using bromide chemical ionisation mass spectrometry, *Atmos. Meas. Tech.*, 12, 891–902, <https://doi.org/10.5194/amt-12-891-2019>, 2019.

- Atkinson, R., Baulch, D. L., Cox, R. A., Crowley, J. N., Hampson, R. F., Hynes, R. G., Jenkin, M. E., Rossi, M. J., and Troe, J.: Evaluated kinetic and photochemical data for atmospheric chemistry: Volume I – gas phase reactions of O_x , HO_x , NO_x and SO_x species, *Atmos. Chem. Phys.*, 4, 1461–1738, <https://doi.org/10.5194/acp-4-1461-2004>, 2004.
- Brauers, T., Aschmutat, U., Brandenburger, U., Dorn, H. P., Hausmann, M., Hessling, M., Hofzumahaus, A., Holland, F., Plass-Dulmer, C., and Ehhalt, D. H.: Intercomparison of tropospheric OH radical measurements by multiple folded long-path laser absorption and laser induced fluorescence, *Geophys. Res. Lett.*, 23, 2545–2548, <https://doi.org/10.1029/96gl02204>, 1996.
- Brauers, T., Hausmann, M., Bister, A., Kraus, A., and Dorn, H. P.: OH radicals in the boundary layer of the Atlantic Ocean I. Measurements by long-path laser absorption spectroscopy, *J. Geophys. Res.*, 106, 7399–7414, <https://doi.org/10.1029/2000jd900679>, 2001.
- Brune, W. H., Stevens, P. S., and Mather, J. H.: Measuring OH and HO_2 in the Troposphere by Laser-Induced Fluorescence at Low-Pressure, *J. Atmos. Sci.*, 52, 3328–3336, [https://doi.org/10.1175/1520-0469\(1995\)052<3328:Moahit>2.0.Co;2](https://doi.org/10.1175/1520-0469(1995)052<3328:Moahit>2.0.Co;2), 1995.
- Burkholder, J. B., Sander, S. P., Abbatt, J., Barker, J. R., Huie, R. E., Kolb, C. E., Kurylo, M. J., Orkin, V. L., Wilmouth, D. M., and Wine, P. H.: Chemical Kinetics and Photochemical Data for Use in Atmospheric Studies, Evaluation No. 18, JPL Publication 15-10, 2015.
- Cantrell, C. A., Edwards, G. D., Stephens, S., Mauldin, L., Kosciuch, E., Zondlo, M., and Eisele, F.: Peroxy radical observations using chemical ionization mass spectrometry during TOPSE, *J. Geophys. Res.*, 108, 8371, <https://doi.org/10.1029/2002JD002715>, 2003.
- COMSOL: Multiphysics Documentation, version 5.4, software, available at: <https://www.comsol.com/>, last access: 30 October 2019.
- Creasey, D. J., Heard, D. E., and Lee, J. D.: Absorption cross-section measurements of water vapour and oxygen at 185 nm. Implications for the calibration of field instruments to measure OH, HO_2 and RO_2 radicals *Geophys. Res. Lett.*, 27, 1651–1654, <https://doi.org/10.1029/1999gl011014>, 2000.
- Creasey, D. J., Evans, G. E., Heard, D. E., and Lee, J. D.: Measurements of OH and HO_2 concentrations in the Southern Ocean marine boundary layer, *J. Geophys. Res.-Atmos.*, 108, 4475, <https://doi.org/10.1029/2002jd003206>, 2003.
- Dieke, G. H. and Crosswhite, H. M.: The Ultraviolet Bands of OH Fundamental Data, *J. Quant. Spectrosc. Ra.*, 2, 97–199, [https://doi.org/10.1016/0022-4073\(62\)90061-4](https://doi.org/10.1016/0022-4073(62)90061-4), 1962.
- Dilecce, G., Ambrico, P. F., and De Benedictis, S.: An ambient air RF low-pressure pulsed discharge as an OH source for LIF calibration, *Plasma Sources Sci. T.*, 13, 237–244, <https://doi.org/10.1088/0963-0252/13/2/007>, 2004.
- Dorn, H. P., Neuroth, R., and Hofzumahaus, A.: Investigation of OH Absorption Cross-Sections of Rotational Transitions in the Band under Atmospheric Conditions: Implications for Tropospheric Long-Path Absorption-Measurements, *J. Geophys. Res.*, 100, 7397–7409, <https://doi.org/10.1029/94JD03323>, 1995.
- Dusanter, S., Vimal, D., and Stevens, P. S.: Technical note: Measuring tropospheric OH and HO_2 by laser-induced fluorescence at low pressure. A comparison of calibration techniques, *At-*

- mos. Chem. Phys., 8, 321–340, <https://doi.org/10.5194/acp-8-321-2008>, 2008.
- Engel, V., Staemmler, V., Vanderwal, R. L., Crim, F. F., Senion, R. J., Hudson, B., Andresen, P., Hennig, S., Weide, K., and Schinke, R.: Photodissociation of Water in the 1st Absorption-Band – a Prototype for Dissociation on a Repulsive Potential-Energy Surface, *J. Phys. Chem.*, 96, 3201–3213, <https://doi.org/10.1021/j100187a007>, 1992.
- Faloon, I. C., Tan, D., Leshner, R. L., Hazen, N. L., Frame, C. L., Simpas, J. B., Harder, H., Martinez, M., Di Carlo, P., Ren, X. R., and Brune, W. H.: A laser-induced fluorescence instrument for detecting tropospheric OH and HO₂: Characteristics and calibration, *J. Atmos. Chem.*, 47, 139–167, <https://doi.org/10.1023/B:JOCH.0000021036.53185.0e>, 2004.
- Freeman, A. J.: Configuration Interaction Study of the Electronic Structure of the Oh Radical by the Atomic and Molecular Orbital Methods, *J. Chem. Phys.*, 28, 230–243, <https://doi.org/10.1063/1.1744098>, 1958.
- Fuchs, H., Bohn, B., Hofzumahaus, A., Holland, F., Lu, K. D., Nehr, S., Rohrer, F., and Wahner, A.: Detection of HO₂ by laser-induced fluorescence: calibration and interferences from RO₂ radicals, *Atmos. Meas. Tech.*, 4, 1209–1225, <https://doi.org/10.5194/amt-4-1209-2011>, 2011.
- Fuchs, H., Tan, Z., Hofzumahaus, A., Broch, S., Dorn, H.-P., Holland, F., K  n  stler, C., Gomm, S., Rohrer, F., Schr  de, S., Tillmann, R., and Wahner, A.: Investigation of potential interferences in the detection of atmospheric RO_x radicals by laser-induced fluorescence under dark conditions, *Atmos. Meas. Tech.*, 9, 1431–1447, <https://doi.org/10.5194/amt-9-1431-2016>, 2016.
- Hard, T. M., George, L. A., and O’Brien, R. J.: Fage Determination of Tropospheric OH and HO₂, *J. Atmos. Sci.*, 52, 3354–3372, [https://doi.org/10.1175/1520-0469\(1995\)052<3354:Fdotha>2.0.Co;2](https://doi.org/10.1175/1520-0469(1995)052<3354:Fdotha>2.0.Co;2), 1995.
- Hard, T. M., George, L. A., and O’Brien, R. J.: An absolute calibration for gas-phase hydroxyl measurements, *Environ. Sci. Technol.*, 36, 1783–1790, <https://doi.org/10.1021/es015646l>, 2002.
- Heard, D. E. and Pilling, M. J.: Measurement of OH and HO₂ in the troposphere, *Chem. Rev.*, 103, 5163–5198, <https://doi.org/10.1021/cr020522s>, 2003.
- Hens, K., Novelli, A., Martinez, M., Auld, J., Axinte, R., Bohn, B., Fischer, H., Ker  nen, P., Kubistin, D., N  lscher, A. C., Oswald, R., Paasonen, P., Pet  j  , T., Regelin, E., Sander, R., Sinha, V., Sipil  , M., Taraborrelli, D., Tatum Ernest, C., Williams, J., Lelieveld, J., and Harder, H.: Observation and modelling of HO_x radicals in a boreal forest, *Atmos. Chem. Phys.*, 14, 8723–8747, <https://doi.org/10.5194/acp-14-8723-2014>, 2014.
- Hofzumahaus, A., Brauers, T., Aschmutat, U., Brandenburger, U., Dorn, H. P., Hausmann, M., Hessling, M., Holland, F., Plass-Dulmer, C., Sedlacek, M., Weber, M., and Ehhalt, D. H.: Reply [to “Comment on ‘The measurement of tropospheric OH radicals by laser-induced fluorescence spectroscopy during the POPCORN field campaign’ by Hofzumahaus et al. and ‘Intercomparison of tropospheric OH radical measurements by multiple folded long-path laser absorption and laser induced fluorescence’ by Brauers et al.”], *Geophys. Res. Lett.*, 24, 3039–3040, <https://doi.org/10.1029/97gl02947>, 1997.
- Holland, F., Hessling, M., and Hofzumahaus, A.: In-Situ Measurement of Tropospheric Oh Radicals by Laser-Induced Fluorescence – a Description of the Kfa Instrument, *J. Atmos. Sci.*, 52, 3393–3401, [https://doi.org/10.1175/1520-0469\(1995\)052<3393:Ismoto>2.0.Co;2](https://doi.org/10.1175/1520-0469(1995)052<3393:Ismoto>2.0.Co;2), 1995.
- Holland, F., Hofzumahaus, A., Schafer, R., Kraus, A., and Patz, H. W.: Measurements of OH and HO₂ radical concentrations and photolysis frequencies during BERLIOZ, *J. Geophys. Res.*, 108, 8246, <https://doi.org/10.1029/2001JD001393>, 2003.
- Ivanov, A. V., Trakhtenberg, S., Bertram, A. K., Gershenzon, Y. M., and Molina, M. J.: OH, HO₂, and ozone gaseous diffusion coefficients, *J. Phys. Chem. A*, 111, 1632–1637, <https://doi.org/10.1021/jp066558w>, 2007.
- Kukui, A., Ancellet, G., and Le Bras, G.: Chemical ionisation mass spectrometer for measurements of OH and Peroxy radical concentrations in moderately polluted atmospheres, *J. Atmos. Chem.*, 61, 133–154, <https://doi.org/10.1007/s10874-009-9130-9>, 2008.
- Langhoff, S. R., Vandishoeck, E. F., Wetmore, R., and Dalgarno, A.: “Radiative Lifetimes and Dipole-Moments of the A²Σ⁺, B²Σ⁺, and C²Σ⁺ States of OH, *J. Chem. Phys.*, 77, 1379–1390, <https://doi.org/10.1063/1.443962>, 1982.
- Lelieveld, J., Peters, W., Dentener, F. J., and Krol, M. C.: Stability of tropospheric hydroxyl chemistry, *J. Geophys. Res.*, 107, 4715, <https://doi.org/10.1029/2002jd002272>, 2002.
- Mallik, C., Tomsche, L., Bourtsoukidis, E., Crowley, J. N., Derstroff, B., Fischer, H., Hafermann, S., H  ser, I., Javed, U., Ke  bel, S., Lelieveld, J., Martinez, M., Meusel, H., Novelli, A., Phillips, G. J., Pozzer, A., Reiffs, A., Sander, R., Taraborrelli, D., Sauvage, C., Schuladen, J., Su, H., Williams, J., and Harder, H.: Oxidation processes in the eastern Mediterranean atmosphere: evidence from the modelling of HO_x measurements over Cyprus, *Atmos. Chem. Phys.*, 18, 10825–10847, <https://doi.org/10.5194/acp-18-10825-2018>, 2018.
- Mao, J., Ren, X., Zhang, L., Van Duin, D. M., Cohen, R. C., Park, J.-H., Goldstein, A. H., Paulot, F., Beaver, M. R., Crounse, J. D., Wennberg, P. O., DiGangi, J. P., Henry, S. B., Keutsch, F. N., Park, C., Schade, G. W., Wolfe, G. M., Thornton, J. A., and Brune, W. H.: Insights into hydroxyl measurements and atmospheric oxidation in a California forest, *Atmos. Chem. Phys.*, 12, 8009–8020, <https://doi.org/10.5194/acp-12-8009-2012>, 2012.
- Marno, D. and Harder, H.: HORUS pressure dependent calibrations using the APACHE calibrator, Data set, Zenodo, <https://doi.org/10.5281/zenodo.3821976>, 2020.
- Martinez, M., Harder, H., Kovacs, T. A., Simpas, J. B., Bassis, J., Leshner, R., Brune, W. H., Frost, G. J., Williams, E. J., Stroud, C. A., Jobson, B. T., Roberts, J. M., Hall, S. R., Shetter, R. E., Wert, B., Fried, A., Alicke, B., Stutz, J., Young, V. L., White, A. B., and Zamora, R. J.: OH and HO₂ concentrations, sources, and loss rates during the Southern Oxidants Study in Nashville, Tennessee, summer 1999, *J. Geophys. Res.*, 108, 4617, <https://doi.org/10.1029/2003jd003551>, 2003.
- Martinez, M., Harder, H., Kubistin, D., Rudolf, M., Bozem, H., Eerdeken, G., Fischer, H., Kl  pfel, T., Gurk, C., K  nigst  dt, R., Parchatka, U., Schiller, C. L., Stickler, A., Williams, J., and Lelieveld, J.: Hydroxyl radicals in the tropical troposphere over the Suriname rainforest: airborne measurements, *Atmos. Chem. Phys.*, 10, 3759–3773, <https://doi.org/10.5194/acp-10-3759-2010>, 2010.
- Mather, J. H., Stevens, P. S., and Brune, W. H.: OH and HO₂ measurements using laser-induced fluorescence, *J. Geophys. Res.*, 102, 6427–6436, <https://doi.org/10.1029/96JD01702>, 1997.

- Mauldin, R. L., Kosciuch, E., Henry, B., Eisele, F. L., Shetter, R., Lefer, B., Chen, G., Davis, D., Huey, G., and Tanner, D.: Measurements of OH, HO₂ + RO₂, H₂SO₄, and MSA at the south pole during ISCAT 2000, *Atmos. Environ.*, 38, 5423–5437, <https://doi.org/10.1016/j.atmosenv.2004.06.031>, 2004.
- Novelli, A., Hens, K., Tatum Ernest, C., Kubistin, D., Regelin, E., Elste, T., Plass-Dülmer, C., Martinez, M., Lelieveld, J., and Harder, H.: Characterisation of an inlet pre-injector laser-induced fluorescence instrument for the measurement of atmospheric hydroxyl radicals, *Atmos. Meas. Tech.*, 7, 3413–3430, <https://doi.org/10.5194/amt-7-3413-2014>, 2014.
- Regelin, E., Harder, H., Martinez, M., Kubistin, D., Tatum Ernest, C., Bozem, H., Klippel, T., Hosaynali-Beygi, Z., Fischer, H., Sander, R., Jücker, P., Königstedt, R., and Lelieveld, J.: HO_x measurements in the summertime upper troposphere over Europe: a comparison of observations to a box model and a 3-D model, *Atmos. Chem. Phys.*, 13, 10703–10720, <https://doi.org/10.5194/acp-13-10703-2013>, 2013.
- Ren, X. R., Harder, H., Martinez, M., Leshner, R. L., Oliger, A., Simpas, J. B., Brune, W. H., Schwab, J. J., Demerjian, K. L., He, Y., Zhou, X. L., and Gao, H. G.: OH and HO₂ chemistry in the urban atmosphere of New York City, *Atmos. Environ.*, 37, 3639–3651, [https://doi.org/10.1016/S1352-2310\(03\)00459-X](https://doi.org/10.1016/S1352-2310(03)00459-X), 2003.
- Roach, P. E.: The Generation of Nearly Isotropic Turbulence by Means of Grids, *Int. J. Heat Fluid Fl.*, 8, 82–92, [https://doi.org/10.1016/0142-727x\(87\)90001-4](https://doi.org/10.1016/0142-727x(87)90001-4), 1987.
- Sander, S. P., Finlayson-Pitts, B. J., Friedl, R. R., Golden, D. M., Huie, R. E., Kolb, C. E., Kurylo, M. J., Molina, M. J., Moortgat, G. K., Orkin, V. L., and Ravishankara, A. R.: Chemical Kinetics and Photochemical Data for Use in Atmospheric Studies, JPL Publication 02-25, 2003.
- Schlosser, E., Bohn, B., Brauers, T., Dorn, H. P., Fuchs, H., Haseler, R., Hofzumahaus, A., Holland, F., Rohrer, F., Rupp, L. O., Siese, M., Tillmann, R., and Wahner, A.: Intercomparison of two hydroxyl radical measurement techniques at the atmosphere simulation chamber SAPHIR, *J. Atmos. Chem.*, 56, 187–205, <https://doi.org/10.1007/s10874-006-9049-3>, 2007.
- Schlosser, E., Brauers, T., Dorn, H.-P., Fuchs, H., Häseler, R., Hofzumahaus, A., Holland, F., Wahner, A., Kanaya, Y., Kajii, Y., Miyamoto, K., Nishida, S., Watanabe, K., Yoshino, A., Kubistin, D., Martinez, M., Rudolf, M., Harder, H., Berresheim, H., Elste, T., Plass-Dülmer, C., Stange, G., and Schurath, U.: Technical Note: Formal blind intercomparison of OH measurements: results from the international campaign HOxComp, *Atmos. Chem. Phys.*, 9, 7923–7948, <https://doi.org/10.5194/acp-9-7923-2009>, 2009.
- Sjostedt, S. J., Huey, L. G., Tanner, D. J., Peischl, J., Chen, G., Dibb, J. E., Lefer, B., Hutterli, M. A., Beyersdorf, A. J., Blake, N. J., Blake, D. R., Sueper, D., Ryerson, T., Burkhardt, J., and Stohl, A.: Observations of hydroxyl and the sum of peroxy radicals at Summit, Greenland during summer 2003, *Atmos. Environ.*, 41, 5122–5137, <https://doi.org/10.1016/j.atmosenv.2006.06.065>, 2007.
- Smith, S. C., Lee, J. D., Bloss, W. J., Johnson, G. P., Ingham, T., and Heard, D. E.: Concentrations of OH and HO₂ radicals during NAMBLEX: measurements and steady state analysis, *Atmos. Chem. Phys.*, 6, 1435–1453, <https://doi.org/10.5194/acp-6-1435-2006>, 2006.
- Stevens, P. S., Mather, J. H., and Brune, W. H.: Measurement of Tropospheric OH and HO₂ by Laser-Induced Fluorescence at Low-Pressure, *J. Geophys. Res.*, 99, 3543–3557, <https://doi.org/10.1029/93JD03342>, 1994.
- Stone, D., Evans, M. J., Commane, R., Ingham, T., Floquet, C. F. A., McQuaid, J. B., Brookes, D. M., Monks, P. S., Purvis, R., Hamilton, J. F., Hopkins, J., Lee, J., Lewis, A. C., Stewart, D., Murphy, J. G., Mills, G., Oram, D., Reeves, C. E., and Heard, D. E.: HO_x observations over West Africa during AMMA: impact of isoprene and NO_x, *Atmos. Chem. Phys.*, 10, 9415–9429, <https://doi.org/10.5194/acp-10-9415-2010>, 2010.
- Tang, M. J., Cox, R. A., and Kalberer, M.: Compilation and evaluation of gas phase diffusion coefficients of reactive trace gases in the atmosphere: volume 1. Inorganic compounds, *Atmos. Chem. Phys.*, 14, 9233–9247, <https://doi.org/10.5194/acp-14-9233-2014>, 2014.
- Tanner, D. J. and Eisele, F. L.: Present OH Measurement Limits and Associated Uncertainties, *J. Geophys. Res.*, 100, 2883–2892, <https://doi.org/10.1029/94JD02609>, 1995.
- Verreycken, T. and Bruggeman, P. J.: OH density measurements in nanosecond pulsed discharges in atmospheric pressure N₂–H₂O mixtures, *Plasma Sources Sci. T.*, 23, 015009, <https://doi.org/10.1088/0963-0252/23/1/015009>, 2014.
- Winiberg, F. A. F., Smith, S. C., Bejan, I., Brumby, C. A., Ingham, T., Malkin, T. L., Orr, S. C., Heard, D. E., and Seakins, P. W.: Pressure-dependent calibration of the OH and HO₂ channels of a FAGE HO_x instrument using the Highly Instrumented Reactor for Atmospheric Chemistry (HIRAC), *Atmos. Meas. Tech.*, 8, 523–540, <https://doi.org/10.5194/amt-8-523-2015>, 2015.
- Zhang, D. H., Collins, M. A., and Lee, S. Y.: First-principles theory for the H + H₂O, D₂O reactions, *Science*, 290, 961–963, <https://doi.org/10.1126/science.290.5493.961>, 2000.